JGR Planets

RESEARCH ARTICLE
10.1029/2018JE005912

Meteoroids at the Moon: Orbital Properties, Surface Vaporization, and Impact Ejecta Production

Petr Pokorný[1,2,3], Diego Janches[2], Menelaos Sarantos[2], Jamey R. Szalay[4], Mihály Horányi[5,6], David Nesvorný[7], and Marc J. Kuchner[3]

[1]Department of Physics, The Catholic University of America, Washington, USA, [2]Heliophysics Science Division, NASA Goddard Space Flight Center, Greenbelt, MD, USA, [3]Astrophysics Science Division, NASA Goddard Space Flight Center, Greenbelt, MD, USA, [4]Department of Astrophysical Sciences, Princeton University, Princeton, NJ, USA, [5]Department of Physics, University of Colorado Boulder, 392 UCB, Boulder, CO, USA, [6]Laboratory for Atmospheric and Space Physics, Boulder, CO, USA, [7]Department of Space Studies, Southwest Research Institute, Boulder, CO, USA

Key Points:
- Novel model characterizes the direction, velocity, and arrival rates of meteoroids with latitude and local time at the Moon during 1 year
- Synthesis of Moon/Earth measurements provides estimates for the lunar meteoroid mass influx, impact vaporization, and ejecta production rate
- Ejecta deposition rates of 30 cm/Myr and reasonable lunar impact vaporization rates result from this approach

Correspondence to:
P. Pokorny,
petr.pokorny@nasa.gov

Citation:
Pokorný, P., Janches, D., Sarantos, M., Szalay, J. R., Horányi, M., Nesvorný, D., & Kuchner, M. J. (2019). Meteoroids at the Moon: Orbital properties, surface vaporization, and impact ejecta production. *Journal of Geophysical Research: Planets*, *124*. https://doi.org/10.1029/2018JE005912

Received 7 JAN 2019
Accepted 21 FEB 2019
Accepted article online 28 FEB 2019

Abstract We use a dynamical model to characterize the monthly and yearly variations of the lunar meteoroid environment for meteoroids originating from short and long-period comets and the main-belt asteroids. Our results show that if we assume the meteoroid mass flux of 43.3 tons per day at Earth, inferred from previous works, the mass flux of meteoroids impacting the Moon is 30 times smaller, approximately 1.4 tons per day, and shows variations of the order of 10% over a year. The mass flux difference is due to the combined effect of the smaller cross-section of the Moon (factor of 13.46) and Earth's larger gravitational focusing (factor of 2–2.5). The lunar surface is vaporized by these impactors at an average impact vaporization flux of 11.6×10^{-16} g·cm^{-2}·s^{-1}, providing a significant source for the rarefied lunar exosphere. Our model predicts acceptable vaporization rates and reproduces the local time dependence of observations of the dust ejecta cloud, measured by the Lunar Dust Experiment on board NASA's Lunar Atmosphere and Dust Environment (LADEE) satellite. However, the predicted density of the lunar ejecta cloud is four orders of magnitude larger than reported values by LADEE. This discrepancy might be attributed to a much lower yield from meteoroid impacts on fluffy lunar regolith and/or a lower detection efficiency of the LADEE dust detector. We suggest an upper limit of 30 cm per million years for the soil gardening rate from small meteoroids.

Plain Language Summary The lunar surface is continuously bombarded by small but fast and abundant particles at rates that amount to 1.4 tons per day. These particles originate from asteroids and comets and after striking the surface produce a variety of observable phenomena such as a thin atmosphere and a dust cloud engulfing our satellite. Our novel model describes for the first time in detail the directions and velocities of particles impacting the Moon, including their variability in time and space. This approach correctly reproduces the shape of the dust cloud that was measured by the Lunar Atmosphere and Dust Environment Explorer mission. However, the density of the dust cloud predicted by this model is thousands of times higher than what was inferred from the measurement. On the other hand, our model provides realistic numbers for the mass of particles delivered daily to the Moon and for the exosphere density, resulting in a disagreement that is yet to be understood.

1. Introduction

Without a thick atmosphere the lunar surface is constantly exposed to meteoroid impacts that excavate the uppermost layers of the lunar regolith, create ejecta dust plumes, and melt, vaporize, and ionize various elements, processes which ultimately contribute to a complex lunar environment. In this manuscript, we aim to address three questions regarding the lunar meteoroid environment: (1) Can we fully reproduce recent observations of the Moon's dust cloud with dynamical meteoroid models calibrated with Earth-based measurements? (2) What is the distribution of meteoroid impacts on the lunar surface along with its temporal variability? (3) What is the best estimate of the mass deposition, impact vaporization, and ejecta mass production rate based on our current knowledge of dynamical meteoroid models?

The history of meteoroid models of Earth's closest neighbor is surprisingly short (Borin et al., 2017; Cremonese et al., 2013). While many authors developed a suite of analytic, engineering, and dynam-

ical models for the Earth (Fentzke & Janches, 2008; McNamara et al., 2004; Nesvorný et al., 2010; Nesvorný, Janches, et al., 2011; Nesvorný, Vokrouhlický, et al., 2011; Pokorný et al., 2014), the Moon itself has not yet been discussed in detail. With the advent of new ground-based and space-borne observations of the Moon there exists new interest in understanding the differences between the lunar and terrestrial meteoroid environments. Like for the case of Mercury (Pokorný et al., 2017, 2018), modeling the meteoroid flux on the Moon is critical for understanding the importance of impact vaporization as a source for the lunar exosphere (Bruno et al., 2007; Cremonese et al., 2013; Morgan et al., 1988; Morgan & Killen, 1997; Sarantos et al., 2012), as meteoroids in the size range of 5–200 μm are considered relevant to the daily resupply of the lunar atmosphere. The importance of impacts for the exosphere was demonstrated by the brightening of its sodium and potassium component during meteor showers (Barbieri et al., 2001; Colaprete et al., 2016; Smith et al., 1999; Szalay et al., 2016).

Reasons to revisit meteoroid models of the Moon were provided when the Lunar Dust Experiment (LDEX) on board the NASA Lunar Atmosphere and Dust Environment Explorer (LADEE) observed lunar ejecta produced by meteoroid impacts during its mission between November 2013 and April 2014 (Horányi et al., 2015; Szalay & Horányi, 2015). The lunar ejecta cloud was found to be persistent in time and asymmetric with respect to Earth's velocity vector direction. Szalay and Horányi (2015) found that, while this asymmetric cloud can be well explained by combining three sources of meteors observed at Earth, the Helion, Antihelion, and Apex sources, the ejecta mass production rate from the Helion source was found to be approximately twice as strong as the Antihelion source (Szalay & Horányi, 2015). Such asymmetry has not been observed in the distribution of meteors measured by radars (Campbell-Brown, 2008; Janches et al., 2015) and optical systems (Jenniskens et al., 2016), although Suggs et al. (2014) suggested an asymmetry in impactor directions for kilogram-sized meteoroids.

The meteoritic flux at the Moon was first estimated with dynamical evolution models of meteoroid particles for the purpose of estimating impact vaporization rates for the lunar exosphere (Borin et al., 2017; Cremonese et al., 2013). These models used only meteoroids originating from main-belt asteroids (MBAs) and Jupiter-family comets (JFCs) and lacked sufficient statistics to give distributions of arrival direction. More recently, Janches et al. (2018) presented a new dynamical model of the lunar meteoroid environment consisting of meteoroids originating from comets for the purpose of interpreting LDEX observations. This effort provided superb spatial resolution of ejecta rates in the reference frame of the Moon and led to several conclusions: (1) a ∼20% contribution to the asymmetry in LDEX measurements is caused by the orientation of the LADEE spacecraft orbit, but in addition to this effect the response of the soil to incoming meteoroids must be different on the lunar dayside and nightside; (2) dynamical meteoroid models could fit monthly ejecta mass production rates determined from LDEX observations reasonably well; and (3) the inferred mass flux ratio between the short and long-period comet (LPC) meteoroids on the Moon was smaller than that reported at Earth (Moon, 1.3:1 vs Earth, 7:1). This finding was interpreted to indicate that the ejecta rate yield is a steeper function of the velocity of the incident meteoroids than assumed before, since LPC particles have on average higher impact velocities than their short-period comet counterparts.

Here, we expand on this effort and probe the effects of various free parameters intrinsic to the dynamical models used both in Janches et al. (2018) and here. In comparing Earth rates and LDEX data we now include the effect of gravitational focusing that plays a significant role in shaping the lunar and terrestrial meteoroid environment. And, finally, we provide calibrated total impact vaporization and ejecta mass production rates as a function of local time (LT) and lunar phase, which will be used in the future as inputs to models of the lunar exosphere.

2. Methods

2.1. Overview of Meteoroid Models

Dynamical models of meteoroids provide a collisionless, steady state distribution of meteoroid populations in the solar system from a limited number of modeled test particles. An inherent assumption is that at steady state a balance is established between the production of meteoroids from their asteroidal and cometary sources, and their removal from the system via different processes such as collisions with planets, escape from the system on unbound orbits or the meteoroid evaporation near the Sun (see, e.g., Nesvorný et al., 2010). During the dynamical lifetime of each modeled meteoroid many snapshots of its orbital state vector

Table 1
Description of Dynamical Models Used in This Manuscript

Source population	Acronym	Diameters modeled (mm)	N particles per diameter	Reference
Main-belt asteroids	MBAs	10, 20, 50, 100, 200, 500 800, 1,000, 1,500, 2,000	20,000	Nesvorný et al. (2010)
Jupiter-family comets	JFCs	10, 30, 50, 100, 200, 500, 800 1,000, 1,200, 1,500, 2,000	100,000	Nesvorný, Janches, et al. (2011)
Halley-type comets	HTCs	10, 20, 50, 100, 200, 400, 600 800, 1,000, 1,200, 1,500, 2,000	20,000	Pokorný et al. (2014)
Oort-Cloud comets	OCCs	10, 20, 50, 100, 200, 400 800, 1,200	20,000	Nesvorný, Vokrouhlický, et al. (2011)

Note. For more detailed information refer to references in the table or Janches et al. (2018) and Pokorný et al. (2018).

are recorded, where each record is considered to be a representation of a unique meteoroid. Then, a simulation that started with an initial population of 10,000 meteoroids can easily result in a steady state system with millions to billions of individual particles, where every one of them has their own orbital state vector, dynamical age, and intrinsic collision probability with all planets. Knowledge of the dynamical age of all records in the simulation allows us to implement collisions after the dynamical evolution of all meteoroids is accounted. The entire meteoroid complex is then constructed from individual meteoroid populations composed of meteoroids of various sizes using assumed size-frequency distributions (SFDs) at the origins to estimate the contribution of different meteoroid sizes.

The dynamical model of meteoroids used in this manuscript consists of four different meteoroid populations originating from MBAs, JFCs, Halley-type comets (HTCs), and Oort-Cloud Comets (OCCs), and is the same as the one used in Pokorný et al. (2018) and (Janches et al., 2018). Since these models have been described extensively in previous works, the reader can follow the references provided in Table 1 for details.

2.2. Mutual Meteoroid Collisions

Grain to grain collisions are one of many processes that can significantly shape the characteristics of the meteoroid complex. Here, for all meteoroid populations we include collisions using a method from Steel and Elford (1986) that allows us to estimate the meteoroid collisional lifetime T_{coll} using the observed number flux of meteoroids in the Zodiacal cloud (i.e., the medium that can cause collisions) and an analytic description of variations of spatial density of meteoroids with heliocentric distance R and ecliptic latitude β. We define T_{coll} as follows:

$$T_{\mathrm{coll}} = \frac{1}{\Sigma\psi(1-\sin\beta)R^{-1.3}\psi_m\sigma_m V_r \Delta U}, \tag{1}$$

where the summation is over the entire meteoroid orbit, ψ is the spatial density of the Zodiacal cloud at 1 au, ψ_m is the spatial density of an investigated meteoroid along its orbit, σ_m is the meteoroid cross-section, V_r is the relative velocity of the mutual collision, and ΔU is the volume element used for the summation. Details of the method can be found in Appendices of Steel and Baggaley (1985) and Steel and Elford (1986).

The spatial density of Zodiacal cloud projectiles at 1 au ψ is derived from *LDEF* (Long-Duration Exposure Facility) measurements which were recently reinvestigated by Cremonese et al. (2012). We digitized the Comets iSALE curve from Figure 2 in Cremonese et al. (2012), converted it from mass to diameter using a bulk density of 2 g cm^{-2}, and converted the cumulative flux to the number density by assuming an average impact velocity of 20 km/s. In the discussion from Steel and Elford (1986) meteoroids 30–40 times smaller in radius can cause catastrophic disruptions of a meteoroid during hypervelocity collisions. Assuming the lower limit, 30, we multiply the radius of projectiles by a factor of 30 in order to get the projectile spatial density ψ at 1 au able to cause catastrophic disruptions of meteoroids smaller than D. Following these steps we obtain the decadic logarithm of the spatial density ψ of projectiles at 1 au that are able to collisionally disrupt meteoroids smaller than diameter D in micrometers by a seventh degree polynomial:

$$\log_{10}(\psi(D)) = a_0 + a_1 D + a_2 D^2 + a_3 D^3 + a_4 D^4 + a_5 D^5 + a_6 D^6 + a_7 D^7, \tag{2}$$

with coefficients: $a_0 = 24.57405$, $a_1 = -0.00274$, $a_2 = 2.42366 \times 10^{-06}$, $a_3 = -1.55354 \times 10^{-09}$, $a_4 = 6.15333 \times 10^{-13}$, $a_5 = -1.42904 \times 10^{-16}$, $a_6 = 1.76861 \times 10^{-20}$, $a_7 = -8.96753 \times 10^{-25}$. The spatial density here is in units of number of meteoroids per au^{-3}, the same units used in Steel and Elford (1986). An independent estimate for ψ by Grun et al. (1985) provides similar estimates where the only difference is that Grun et al. (1985) predicts more collisions (factor of ~5) for meteoroids with $D < 40$ μm by including a population of β-meteoroids. Meteoroids with $D < 50$ μm are not significantly disrupted by this process of "collisional grooming" in our models (Pokorný et al., 2018) which makes the results of this paper robust to different estimates of meteoroid spatial densities at 1 au. The assumed spatial density of projectiles in the inner solar system follow the heliocentric distance variations $\psi \propto r^{-1.3}$ inferred from HELIOS A/B spacecraft measurements (Leinert et al., 1981), while the ecliptic latitude assumption comes from Steel and Elford (1986).

The collisional lifetimes thus obtained in the inner solar system are too short in order to properly reproduce orbital element distributions observed by radars at Earth (e.g., Nesvorný, Janches, et al., 2011; Pokorný et al., 2014) . This finding resulted in the adoption of a scaling factor F_{coll} that multiplies the nominal (i.e., derived from observations) collisional lifetime in order to match the observations. Then $T_{\mathrm{coll}_{\mathrm{new}}} = T_{\mathrm{coll}} * F_{\mathrm{coll}}$, where Pokorný et al. (2014) tested F_{coll} for values from 1 to 50 inferring that the best fit was obtained with $F_{\mathrm{coll}} = 20$. Several reasons might explain why F_{coll} is much larger than unity. Meteoroids might be structurally stronger than assumed, relative collision velocities might be smaller beyond 1 au, or the porosity of meteoroid grains might dampen the effect of smaller projectiles. However, without proper laboratory experiments or in situ calibrations the reason for this discrepancy is currently unknown. Note that for $F_{\mathrm{coll}} > 100$ mutual meteoroid collisions are infrequent and the model outcome is very similar to a collisionless model except for the meteoroids with $D>$ 1 mm. Because the full description of collisional grooming of all meteoroid population models is beyond the scope of this manuscript we refer the reader to Pokorný et al. (2018) who studied in detail collisional effects on meteoroids for meteoroids impacting Mercury.

Recently, new collisional methods were developed in order to treat collisions in a more self-consistent manner (e.g., Kuchner & Stark, 2010). We did not implement these methods for two reasons: (1) no method with ability to process the amount of meteoroids in our models is currently available and (2) if we applied a new collisional algorithm, we would need to reanalyze how well these new models fit existing data sets, which is beyond the scope of this manuscript. Implementation of more sophisticated collisional mechanisms is planned for future work.

The effects of collisions are applied at each record time step T_{step} in such a way that we decrease the collisional weight of each meteoroid W_c to a new value $W_c^{\mathrm{new}} = W_c * \exp(-T_{\mathrm{step}}/T_{\mathrm{coll}})$ to describe the probability of survival. W_c is initially set to 100% and is consequently decreased while meteoroids dynamically evolve.

2.3. Meteoroid Impact Probability With Planets

Even with billions of simulated records of meteoroid orbital state vectors, the number of direct impacts on planets is negligible in our simulations since the number of simulated meteoroids is limited and the impact probability is extremely small due to the vastness of the space and small target cross-sections. Fortunately, many diverse methods were developed in order to estimate the collision probability between two objects in the solar system (Greenberg, 1982; Kessler, 1981; Pokorný & Vokrouhlický, 2013; Öpik, 1951; Vokrouhlický et al., 2012; Wetherill, 1967). In this work we adopted a formalism proposed by Kessler (1981), which allows us to estimate changes in the lunar meteoroid environment on daily and monthly timescales. This is because Kessler's method allows a choice of the target's (i.e., lunar) position and velocity, unlike other methods which require orbital elements. And even though Rickman et al. (2014) showed that Kessler's method can lead to overestimation of collisional probabilities due to singularities arising from particular orbital configurations, the large number of particles used in our implementation of Kessler's method outweighs such limitations.

In this model we account for the gravitational focusing effect on the collisional cross-section area σ, an effect omitted in Janches et al. (2018). Following Öpik (1951) we define

$$\sigma = \pi(r_1 + r_2)^2 \left[1 + \frac{V_{\mathrm{esc}}^2}{V_{\mathrm{rel}}^2 + \epsilon^2}\right], \tag{3}$$

where r_1 and r_2 are projectile's and target's average radii, V_{esc} is the escape velocity of the more massive object (i.e., the target), V_{rel} is the relative velocity of the two objects, and ϵ is a softening parameter. Note, that

$r_2 \ll r_1$, so for simplicity we can assume $r_2 = 0$ in equation 3. As shown by Kortenkamp (2013) particles captured in quasi-satellite orbits can lead to extremely high values of σ due to minimal target-projectile relative velocities. For that reason we choose $\epsilon = 0.1$ km/s. This allows us to avoid overestimating the effect of gravitational focusing resulting from individual particles in our model. We tested the sensitivity of our results to other values, $\epsilon = 0.01, 0.05$, and found that the change of ϵ had negligible impact on the outcome of our dynamical model. The importance of including gravitational focusing was emphasized in Kortenkamp (2013) who showed that omitting this effect can lead to mass fluxes at Earth that are orders of magnitude smaller for certain populations of dust particles in the inner solar system. Gravitational focusing of low velocity meteoroids by the Moon is less pronounced due to the lunar lower escape velocity, $V_{esc} = 2.4$ km/s, as opposed to $V_{esc} = 11.2$ km/s for Earth. We include gravitational focusing from both the Earth and Moon in our model.

In this work we analyze the lunar meteoroid environment for a period of one Earth year from 1 July 2013 at 00:00 UTC until 1 July 2014 at 00:00 UTC, to overlap with LADEE. The model outcome is recalculated every 12 hr thus sampling the meteoroid environment at 731 positions of the Moon uniformly separated in time. The orbital elements of the Moon were taken from JPL HORIZONS Web-Interface for Target body: Moon [Luna] (301), Center body: Sun (10), DE431mx. The collisional probability is evaluated for each of the 731 time frames separately in order to capture small changes of the lunar meteoroid environment in this period.

2.4. SFD

The distribution of sizes of meteoroids in the meteoroid complex is one of the most important characteristics in all dynamical models. Once released from their parent bodies, meteoroids of different sizes undergo different dynamical evolution due to the nature of radiative forces. Smaller meteoroids are more efficiently dragged by PR drag into the Sun, which causes a change of the initial SFD. In models presented here the SFD is always assumed at the source, that is, the SFD right after meteoroids left their parent bodies. That is, the SFD at the source is a model input, whereas the SFD at Earth or the Moon is a model output. The SFD can be approximated by many different forms, but here for simplicity we describe the source SFD using a single power law. The number of meteoroids dN per size (diameter) bin dD is expressed as

$$\mathrm{d}N \propto D^{-\alpha}\mathrm{d}D. \tag{4}$$

The exponent α in equation (4) is then the differential size index at the source. This equation can be integrated to obtain the number of meteoroids within the diameter range (D_1, D_2):

$$N(D,\alpha) \propto \int_{D_1}^{D_2} D^{-\alpha}\mathrm{d}D = \frac{1}{\alpha-1}\left[D_2^{-(\alpha-1)} - D_1^{-(\alpha-1)}\right], \tag{5}$$

Having four different meteoroid population requires prescribing four different size indexes in our model. To simplify the matter we assign all populations the same initial size index α and keep it as a free parameter.

Measurements of initial SFDs for any meteoroid population in the solar system are very scarce. Recent observations of 67P/C-G coma by the *Rosetta* mission showed complex variations of SFD with the position in the orbit (Fulle et al., 2016; Rotundi et al., 2015). Larger meteoroids with $D > 1$ mm showed small variations of the size index $\alpha = 4$, while for smaller meteoroids $\alpha = 2$ at comet's aphelion and increased to $\alpha = 3.7$ at perihelion. *Rosetta* observed increased activity close to the comet's perihelion thus we can assume that a large portion of meteoroids are released with steeper SFDs. Similar values for $\alpha \sim 4$ were reported from the *Stardust* mission to 81P/Wild (JFC; Green et al., 2007), and from the *Giotto* mission to 1P/Halley (Fulle et al., 1995). Dohnanyi (1969) showed that any system that reached collisional equilibrium has $\alpha = 3.5$.

Numerous experiments and observations of meteoroid SFDs were performed at 1 au. All meteoroid populations modeled here undergo significant dynamical evolution before the majority of particles can impact objects at 1 au. PR drag, with dynamical timescales $\propto 1/D$ (Burns et al., 1979), decreases α by unity, that is, it makes the SFD shallower. Note that the close-encounters with planets, trappings in mean-motion resonances, or effects of secular resonances have more complex influence on SFDs, because these effects vary for different populations. Grun et al. (1985) provided an excellent compilation of available measurements at that date and for size ranges treated in this manuscript reported $\alpha = 5.05$. Shallower size indexes were reported from the latest meteor radar and optical measurements at Earth that suggest $\alpha = 4.51 \pm 0.21$ (Blaauw et al.,

2011) and $\alpha = 4.30 \pm 0.28$ (Pokorný & Brown, 2016). An excellent measurement of SFD from low Earth orbit was performed by the *LDEF* spacecraft (Love & Brownlee, 1993) , which recorded impact cratering statistics for 5.7 years. However, the conversion of this cratering record to SFD information is very complex. Cremonese et al. (2012) used hydrocode modeling of the cratering process to derive from LDEF data a complex SFD which can be approximated with two power laws; $\alpha = 8.8$ for meteoroids with $D > 200$ μm and $\alpha = 2.8$ for $D < 200$ μm. One source of discrepancy might be a different size range observed by *LDEF* and radar and optical meteor systems. Data in Cremonese et al. (2012) show a very steep distribution for meteoroids with $D > 200$ μm and no impacts from particles with $D > 400$ μm, whereas radars and optical systems observe meteors show more complete data sets for $D > 400$ μm (see, e.g., Pokorný & Brown, 2016).

Given these uncertainties and the scarcity of in situ measurements we evaluated our model for a wide range of size indexes, where $\alpha \in [3.4, 4.6]$. We tested higher values of α for different populations and further increasing α above 4.6 yielded insignificant differences in our model. The same effect was observed with similar dynamical models at Mercury (Pokorný et al., 2018).

2.5. Impact Vaporization and Impact Mass Production Rate

When a meteoroid impacts the surface of the Moon, there are three possible scenarios of the surface reaction depending on its kinetic energy E: (1) E is large enough to melt the surface, (2) E reaches a material dependent threshold and the surface layer vaporizes, and (3) E is so large that plasma comprises a significant fraction of the total vapor (see, e.g., Figure 2 in Cintala, 1992). For the purpose of calculating the vaporization rate we adopt results from the impact vaporization experiment reported by Cintala (1992):

$$\mathcal{M}_{\text{vapor}} = \mathcal{V}_{\text{vapor}}\rho_{\text{vapor}} = \sum \mathcal{V}_{\text{Met}}\rho_{\text{vapor}}(c + dV_{\text{imp}} + eV_{\text{imp}}^2), \tag{6}$$

where $\mathcal{M}_{\text{vapor}}$ is the total vaporized mass, $\mathcal{V}_{\text{vapor}}$ is the volume vaporized by a meteoroid with volume $\mathcal{V}_{\text{Met}}$, $\rho_{\text{vapor}} = 1,500$ kg/m^3 is the bulk density of the vaporized surface, and $c = -3.33$, $d = -0.0102$ km/s, $e = 0.0604$ km^2/s^2 are empirically determined constants from Cintala (1992). For $V_{\text{imp}} < 7.51$ km/s equation (6) gives negative values, thus we set our impact vaporization threshold to $V_{\text{imp}} = 7.51$ km/s. From $\mathcal{M}_{\text{vapor}}$ we can easily derive the impact vaporization flux

$$\mathcal{F} = \frac{\mathcal{M}_{\text{vapor}}}{St}, \tag{7}$$

where S is the surface area that produces $\mathcal{M}_{\text{vapor}}$ over a period of time t. Other authors provide different estimates for the impact vaporization scaling; Borkowski and Dwek (1995) report no vaporization below 30 km/s, while Collette et al. (2014) show that vapor can be observed for impact velocities down to 2 km/s. Impact vaporization experiments have neither been performed for the velocity and size range of realistic impacting meteoroids nor for impactors impinging on material similar to the lunar surface.

Another reaction of the surface to meteoroid impacts is the creation of ejecta. To estimate the mass of ejecta produced by impacts, M^+, we use the empirical formula for mass production rate inspired by Koschny and Grün (2001)

$$M^+ = \sum^{m_{\text{imp}}} C m_{\text{imp}}^{\gamma_1} (v_{\text{imp}}^2)^{\gamma_2} \cos^2\mathcal{A}, \tag{8}$$

where C is a material related constant (see equation 9 in Krivov et al., 2003), m_{imp} is the mass of the impactor, V_{imp} is its impact velocity, γ_1 and γ_2 are experimentally determined indices, and $\mathcal{A}$ is the angular distance from the zenith/impact angle from the surface normal, where the angular dependence $\cos^2\mathcal{A}$ was reported by Gault (1973). Koschny and Grün (2001) provided m_{imp}, V_{imp}, and M^+ for 41 different experiment runs, which allows us to test the sensitivity of our results to γ_1 and γ_2. Note that Koschny and Grün (2001) found $\gamma_1 = \gamma_2 = 1.23$, yet they did not provide any estimate of the uncertainty on these power indices. Koschny and Grün (2001) cautioned that their experiment was performed for a limited range of impact velocities (approximately $V_{\text{imp}} < 7$ km/s) and thus their relation might not be valid outside this range. Even though we will show that the impact velocities of OCC meteoroids can easily exceed 60 km/s, we adopt the original formula for the entire range of impact velocities produced by our model due to the absence of similar experiments for larger impact velocities.

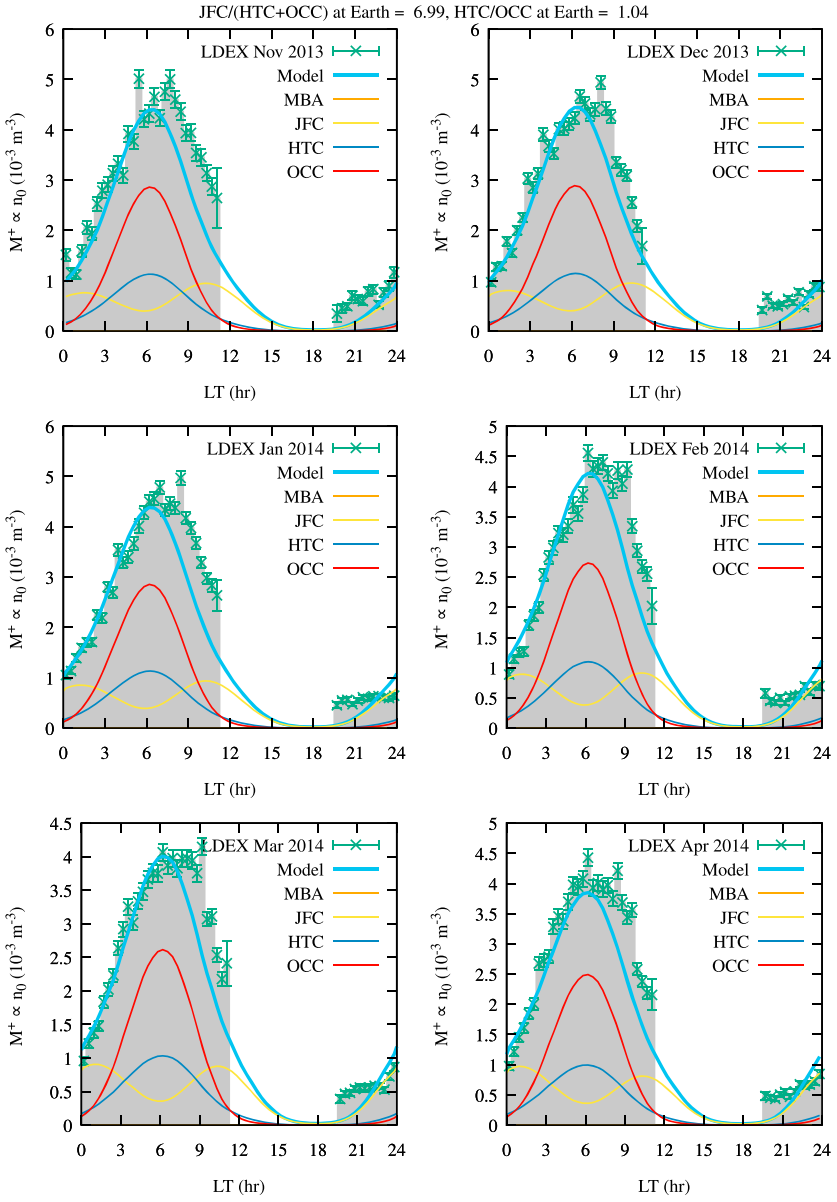

Figure 1. LDEX data for November 2013 to April 2014 (green points with error bars) compared to our model M^+, where the sum of the four populations is represented by the blue solid line. Contributions of individual meteoroid populations are represented by solid lines: MBA (orange), JFC (yellow), HTC (blue), OCC (red). The model was fitting LDEX observations only for LT between 0 and 6 hr. We selected a fit representing a JFC-to-LPC mass ratio at Earth equal to 6.99, and the HTC/OCC mass influx ratio at Earth equal to 1.04. The free parameters used here are: $F_{\mathrm{coll}} = 20, \alpha = 4, \gamma = 1.23$. This is just one out of many representations of our model with a similar goodness of fit ($\chi^2 = 7.99$). The MBA contribution is negligible and thus the orange line is not visible. MBA = main-belt asteroid; JFC = Jupiter-Family Comet; HTC = Halley-type comet; OCC = Oort-Cloud Comet; LDEX = Lunar Dust Experiment; LT = local time.

3. Constraining the Model With LADEE/LDEX Observations

In this Section, we refine the initial analysis presented by Janches et al. (2018), who performed the first comparison between the predictions of dynamical meteoroid models and LDEX dust counter observations. Empirical fits of analytically prescribed meteoroid sources were previously performed by Szalay and Horányi (2015). Specifically, in this work we expand our investigation by (1) including the contributions of meteoroids from asteroid sources and (2) exploring the influence of the following free parameters: collisional lifetime multiplier $F_{\mathrm{coll}} = 10, 20, 50$; SFD index $\alpha = 3.4, 4.0, 4.6$; and $\gamma_1 = \gamma_2 = 1.15, 1.2, 1.23, 1.25, 1.3$ in equation (8). Like in Janches et al. (2018) the LDEX data used here are corrected for observational biases

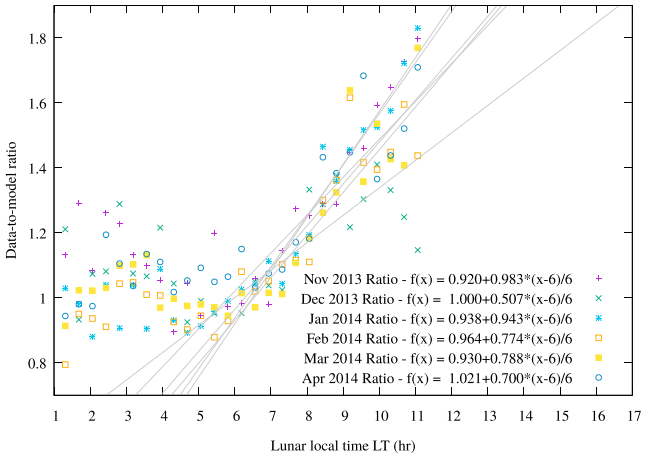

Figure 2. Variations of data-to-model ratios as a function of local time for values from Figure 1, where different months are now denoted with different symbols and colors. Solid gray lines represent linear fits for individual months. The legend shows individual linear fit coefficients. We see that all months show a similar residual trend suggesting a physical nature rather than an observational bias or a systematic error.

such as changes in altitude or measurement cadence (Szalay et al., 2018; Szalay & Horányi, 2016), but for this work the data set is calculated at a higher temporal resolution of 0.375 hr (22.5 min) in lunar LT, which translates to 5.625 longitude degree bins along the LADEE orbit. We focus on monthly averages in order to decrease the intrinsic data noise present in daily or weekly means. We use our dynamical model to estimate the ejecta mass production rate M^+ every 30 s using the LADEE trajectory obtained via the SPICE toolkit (see https://naif.jpl.nasa.gov for more details) and construct monthly averages in the same manner as we calculate the LDEX data, that is, using a temporal resolution of 0.375 hr.

We use the Bayesian inference tool `MultiNest` (Feroz et al., 2009, 2013; Feroz & Hobson, 2008) to obtain the best fit of our model to the data (i.e., posterior probability distribution) for each combination of $F_{\mathrm{coll}}, \alpha, \gamma_1,$ and γ_2. The log-likelihood used in our Bayesian fitting procedure is a reduced chi-squared statistic

$$\log_e \mathcal{L} = -\chi^2 = -\frac{1}{\nu}\sum_i \frac{(O_i - M_i)^2}{\sigma_i^2}, \tag{9}$$

where ν is the degrees of freedom, O_i represents the data points derived from the LDEX observations, σ_i is their variance, M_i is our model prediction, and the summation is applied for all values available from November 2013 to April 2014 a total of 252 values, 42 per each month.

3.1. A Dayside Dependence of the Ejecta Yield

As in Janches et al. (2018) we were not able to obtain a reasonable fit when combining the nightside (LT between 18 and 6 hr) and the dayside (LT between 6 and 18 hr) observations for any combination of free parameters in our model. Specifically, our dynamical model consists of two distinctive sources of M^+:M^+ contribution originating from HTC and OCC meteoroid impacts, with peaks around LT = 6 hr, and impacts from MBA and JFC meteoroids with peaks approximately at LT = 1.5 hr and 10.5 hr. Both peaks produced by MBA/JFC meteoroids have comparable strengths (i.e., the LT = 1.5 hr peak is of similar strength as the 10.5 hr peak). Then, any combination of these two contributions fails to reproduce the dayside enhancement in M^+ previously reported by LDEX (Szalay & Horányi, 2015), with the dynamical model predicting the peak in M^+ to be earlier in LT (LT = 06 hr) as compared to the data (LT ~ 07–08 hr).

While Szalay and Horányi (2015) argue that the observed imbalance between the dayside and nightside ejecta cloud may be due to differences in the incoming meteoroid flux, in particular, those originating from the helion and antihelion sources, Janches et al. (2018), using a preliminary version of the model presented here, suggested that the increased production of ejecta on the lunar dayside is most likely due to yet unrecognized effects of the instrument or, more likely, of the ejecta yield. These effects may include a dependence of M^+ on the surface temperature, and exposure to UV radiation or solar wind.

To further explore the source of this nightside/dayside imbalance, we forced the fitting procedure to work only with the nightside part of the LDEX observations, and calculated the data-to-model ratio. Figure 1 shows the best nightside fit with the JFC-to-LPC mass flux ratio at Earth of 6.99 (i.e., the value suggested by Carrillo-Sánchez et al., 2016) and mass flux ratio at Earth HTC/OCC = 1.04, which we selected to show here due to its similarity to the values used in Janches et al. (2018). Here, LPC = (HTC + OCC) stands for LPC meteoroids. It is important to note that these values are representing population ratios at Earth, as opposed to the ratios presented in Janches et al. (2018) which were estimated at the Moon. Both ratios are related through effects of gravitational focusing. Readily, we see in this figure that the modeled M^+ is experiencing a deficiency on the dayside for all months of LADEE mission. When we force our fitting procedure to fit only the dayside a similar deficiency is present on the nightside, however in this case an overabundance of M^+.

This deficiency is even more evident in Figure 2, where the data-to-model ratio is displayed as a function of lunar LT for the six months of LADEE science operations. The difference between data and model is ~10% or less before 06:00 LT. However, at later times a linear fit appears to describe reasonably well the increase of the data-to-model ratio. Note that, even though the results in Figures 1 and 2 show only one realization of

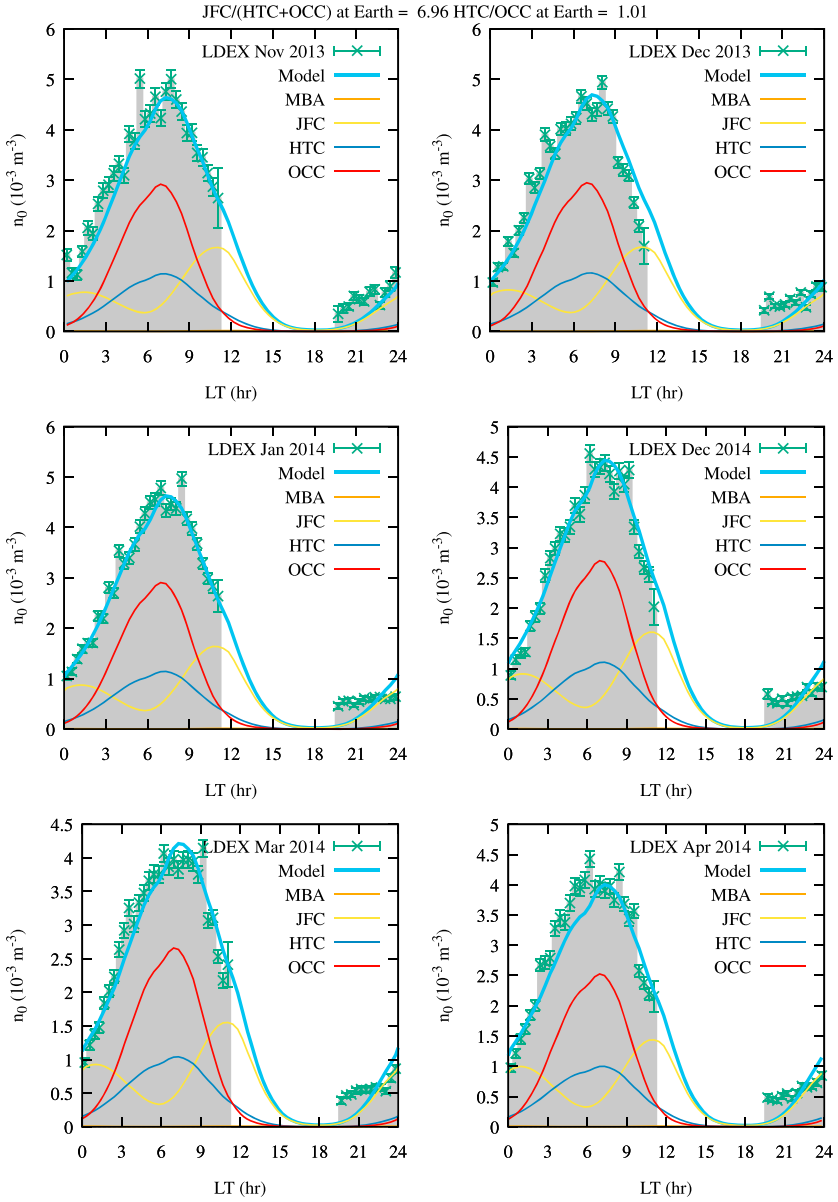

Figure 3. Same as Figure 1, but including the hypothesized increased production rate of ejecta in the dayside ($\Psi = 81\%$). A reduced $\chi^2 = 2.3$ was obtained in this case with free parameters: $F_{\rm coll} = 20, \alpha = 4, \gamma = 1.23$.

our model ($F_{\rm coll} = 20, \alpha = 4, \gamma_1 = 1, \gamma_2 = 1.25$), this trend is present in all model realizations we explored in this manuscript. Two main conclusions can be drawn from this exercise: first, the data-to-model ratio on the dayside depends on LT and is increasing linearly from LT = 6 to 12 hr; and second, this behavior is consistent throughout the entire mission, suggesting a systematic offset of the LDEX instrument data caused by for example, increasing temperature on the dayside, or the variation of M^+ with LT.

To account for this effect we propose a modified version of equation (8) by including a term given by

$$\begin{aligned} |LT-12| > 6 &: M^+ = \sum^{m_{\rm imp}} C m_{\rm imp}^{\gamma_1} (v_{\rm imp}^2)^{\gamma_2} \\ |LT-12| \le 6 &: M^+ = \sum^{m_{\rm imp}} C m_{\rm imp}^{\gamma_1} (v_{\rm imp}^2)^{\gamma_2} \times [1 + \Psi(1 - |12 - LT|/6)], \end{aligned} \tag{10}$$

where $\Psi \in [0:1]$ is the fractional increase between LT = 6 and 12 hr. Note that there is also a symmetric decrease from LT = 12 to 18 hr. With this formulation the maximum increase of M^+ at LT = 12 hr is 100%

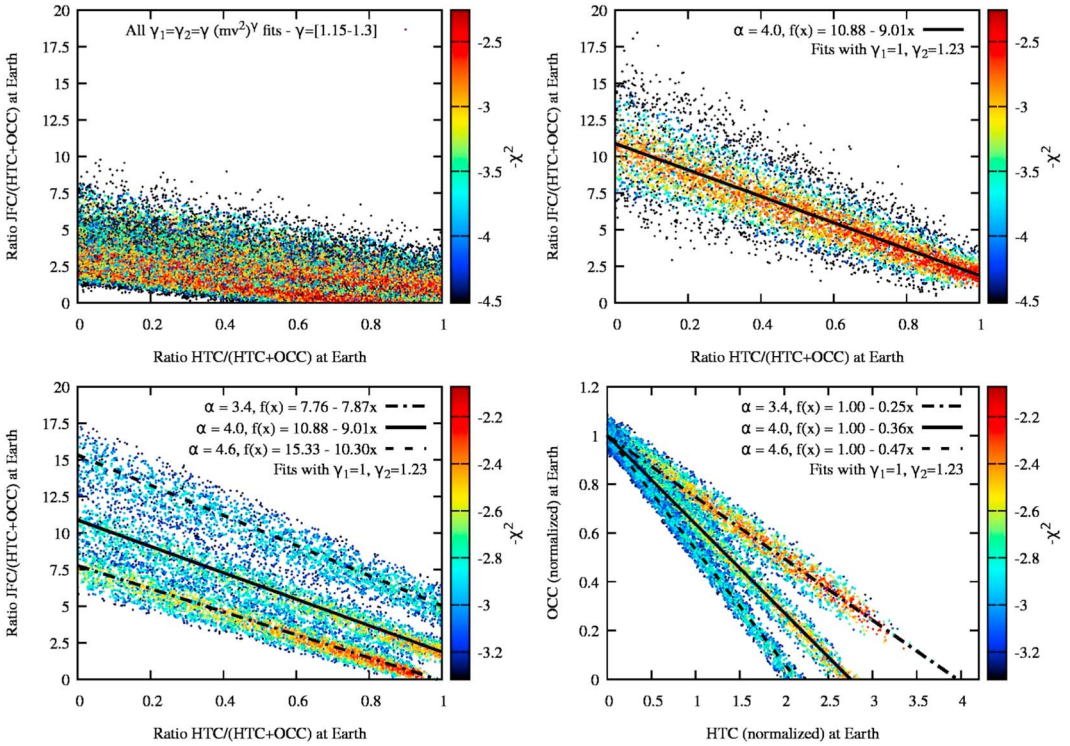

Figure 4. Correlations between different quantities resulting from our Multinest fitting procedure. All plots are color coded with $\log_e \mathcal{L} = -\chi^2$, showing the goodness of the fit. (top left) Ratio between the JFC and (HTC + OCC) mass flux at Earth versus the fraction of HTC meteoroids in the total mass flux of long-period comet = (HTC + OCC) meteoroids at Earth for all combinations of the following free parameters $F_{\mathrm{coll}} = (10, 20, 50), \alpha = (3.4, 4.0, 4.6), \gamma_1 = \gamma_2 = (1.15, 1.2, 1.23, 1.25, 1.3)$, where $\gamma_1 = \gamma_2 = 1.23$ is value from Koschny and Grün (2001). (top right) The same as top left panel but now for $F_{\mathrm{coll}} = 20, \alpha = 4, \gamma_1 = 1, \gamma_2 = 1.23$. The subtle change in $\gamma_1 = 1$ significantly changes the posterior distribution. The black solid line represents a linear fit to the posterior distribution and the goodness of fit along it is similar. (bottom left) The same as top right panel but now for three different values of $\alpha = 3.4, 4.0, 4.6$. The color scale was changed to avoid overlapping between different model realizations. Different line types refer to different values of α. (bottom right) Mass flux at Earth of OCC meteoroids at Earth versus the mass flux of HTC meteoroids at Earth. Both axes are normalized to one mass unit of OCC meteoroids at Earth (using the linear fit for each model separately). JFC = Jupiter-Family Comet; HTC = Halley-type comet; OCC = Oort-Cloud Comet.

and Ψ is now an additional parameter to be fitted by our Bayesian fitting procedure. Figure 3 shows the best fit for the JFC-to-LPC mass flux ratio at Earth = 6.92, collisional lifetime $F_{\mathrm{coll}} = 20$, and SFD index $\alpha = 4$. There is a noticeable improvement in the quality of the fit, where now our M^+ calculated using our dynamical model reasonably fits all 6 months of LDEX observations. The χ^2 value decreased from 8.1 to 2.5 by introducing the correction in equation (10), which is a significant improvement despite our addition of one free parameter (i.e., a decrease in the number of degrees of freedom).

3.2. Ratio of Meteoroid Populations Constrained by Ejecta Cloud Measurements

Thus, revised to account for an increased yield on the dayside, our model can now provide new insights about the relative ratios of meteoroid populations at 1 au. Note that currently the LDEX observations do not provide absolute values of M^+ and thus we cannot yet obtain the absolute values of the mass flux at Earth for individual meteoroid populations using this measurement. In this work we choose to reference the resulting ratios of the different meteoroid populations at Earth whereas Janches et al. (2018) reported population ratios at the Moon. Our choice is driven by the fact that direct meteoroid observations obtained near the Moon or other solar system bodies are scarce compared to those at Earth.

Figure 4 shows the posterior distributions of our dynamical model fits. The top left panel in Figure 4 shows the relationship between the fraction of HTC meteoroids to the whole budget of LPCs (HTCs + OCCs) and the JFC-to-LPC ratio, that is, the mass flux of short and LPC meteoroids when $\gamma_1 = \gamma_2$. We show the posterior distributions for all combinations of the following free parameters: $F_{\mathrm{coll}} = (10, 20, 50), \alpha =$

$(3.4, 4.0, 4.6), \gamma_1 = \gamma_2 = (1.15, 1.2, 1.23, 1.25, 1.3)$, where $\gamma_1 = \gamma_2 = 1.23$ is the value from Koschny and Grün (2001). The color scale in this figure represents $\log_e \mathcal{L}$, in our case the negative value of the reduced χ^2, that is, values closer to 0 provide better fit. Carrillo-Sánchez et al. (2016) suggests that the JFC-to-LPC mass flux ratio at Earth is ~7, which, based on the posterior distribution in the top left panel in Figure 4, is possible only when the HTC fraction is close to 0, which would mean that the meteoroid mass flux of LPCs at Earth is entirely dominated by OCC meteoroids. This is unlikely because Earth-based radar and optical meteor observations indicate that HTC meteoroids are of similar or higher abundance compared to OCC meteoroids (Campbell-Brown, 2008; Janches et al., 2015; Jenniskens et al., 2016; Pokorný et al., 2014).

Based on our tests of equation (8) we find that the retrieved ratios of different populations are significantly more sensitive to changes of the assumed dependence of the ejecta yield on meteoroid mass (γ_1) than to the dependence on velocity (γ_2). Lower values of γ_1 provide a JFC-to-LPC ratio similar to those expected at Earth. This dependence follows from the dynamical evolution of meteoroids in the solar system and the mass segregation for certain meteoroid populations. JFC meteoroids start on orbits already decoupled from Jupiter and thus their SFD at Earth is mostly governed by PR drag that forces the smaller meteoroids to spiral faster toward the Sun. This results in the mass distribution of JFC meteoroids at Earth that is abundant with larger meteoroids ($D > 1{,}000$ μm). On the other hand, HTC and OCC meteoroids have to pass the Jupiter barrier in order to decouple from Jupiter and increase their probability to hit the Earth/Moon (Nesvorný, Vokrouhlický, et al., 2011; Pokorný et al., 2018, 2014). Since the larger meteoroids spend more time in Jupiter crossing orbits, they are scattered more easily and consequently the mass distribution of LPC meteoroids at Earth is dominated by smaller grains: the characteristic size for HTC meteoroids at Earth is $D \sim 100$–200 μm and for OCC meteoroids $D \sim 20$ μm. Then for $\gamma_1 > 1$ this mass segregation effect can introduce a factor of 10–20 difference in M^+ between JFC and LPC meteoroids. Thus, the assumption ($\gamma_1 > 1$) overemphasizes the importance of JFCs in the production of ejecta.

What occurs then if, inspired by the linear dependence of total vapor to the meteoroid mass, we assume $\gamma_1 = 1$ so that M^+ also scales linearly with the mass flux and does not strongly depend on the mass of individual meteoroids? The top right panel in Figure 4 shows the results for our dynamical model with $F_{\mathrm{coll}} = 20, \alpha = 4, \gamma_1 = 1, \gamma_2 = 1.23$. It is readily apparent that the resulting fit allows for higher JFC-to-LPC mass flux ratios than in the previous case. Although the majority of posterior values are concentrated around an HTC fraction ~80%, the quality of the fit is the same along the fitted linear function (solid black line). This means that both solutions, one with no HTC meteoroids or one with no OCC meteoroids, result in the same goodness of fit. The posterior distribution does not change significantly with F_{coll}, and is slightly sensitive to changes in γ_2, where larger values of γ_2 force the posterior distribution to move upward in the plot, that is, to fit properly LDEX data we need more JFC meteoroids. This is due to smaller impact velocities of JFC meteoroids as compared to LPC meteoroids. Janches et al. (2018) showed that increasing γ_2 to 1.75 can produce a factor of 4–5 increase in the JFC-to-LPC mass flux ratio.

The sensitivity of our dynamical model fits to the SFD index α is quantified in the bottom left panel in Figure 4. It can be observed from this figure that for $\alpha = 3.4$ our model can reproduce the LT distribution of M^+ observed by LDEX even for a scenario where there is no contribution from either JFC or OCC meteoroids, with HTC meteoroids being the sole source of lunar surface impacting meteoroids. However, decades of Earth-based observations, ground-based observations, and dynamical modeling have demonstrated that the fluxes of both JFC and OCC meteoroids should represent a significant portion of the incoming meteoroid flux at Earth (Campbell-Brown, 2008; Fentzke & Janches, 2008; Janches et al., 2015; Nesvorný, Janches, et al., 2011; Nesvorný, Vokrouhlický, et al., 2011). Furthermore, Carrillo-Sánchez et al. (2016) required a JFC-to-LPC ratio at Earth of $\sim 6.92^{+14}_{-4.8}$ in order to simultaneously reproduce lidar observations of the vertical Na and Fe fluxes above 87.5 km and the measured cosmic spherule accretion rate at the South Pole. This implies that the LDEX observations alone cannot uniquely constrain the different meteoroid populations considered here at 1 au. The conclusion that LDEX results cannot uniquely constrain the relative flux contributions of different meteoroid populations is further supported by the results shown in the bottom right panel in Figure 4, where both axes are normalized to one mass unit of OCC meteoroids at Earth. OCC meteoroids provide more M^+ per unit mass than HTC meteoroids for any combination of free parameters tested here. OCC meteoroids have higher impact velocities (Nesvorný, Vokrouhlický, et al., 2011), thus providing more M^+ per unit mass than HTC meteoroids which have a significant portion of their population composed of prograde (and thus slower) meteoroids (Pokorný et al., 2014). In addition, with increasing α (i.e., when the mass becomes dominated by smaller meteoroids) the HTC meteoroid contribution to M^+

becomes more comparable to that produced by OCC meteoroids. The changes of the slope value in the bottom right panel caused by variation of other free parameters (F_{coll} and γ) are in units of percents. The LT enhancement Ψ from equation (10) between LT = 6 and 12 hr provides the best fits for values in the range $\Psi = [0.65,0.85]$, regardless of which combination of free parameters is used.

Whereas LDEX measurements are unable to provide a unique absolute calibration for different meteoroid populations around Earth, one thing is clear: due to their very slow impact velocities, the contribution of MBA meteoroids to the total budget of M^+ is negligible as compared to cometary meteoroid populations. For the remaining populations, JFC, HTC, and OCC meteoroids, we observe a large solution space mostly due to the one dimensional nature of LDEX observations. However, if a reference value is selected, for example, JFC mass flux at Earth is $\mathcal{M}_{JFC} = 34.6$ t/day and JFC-to-LPC ratio = 6.92 following Carrillo-Sánchez et al. (2016), we obtain a mass flux at Earth of HTC meteoroids $\mathcal{M}_{HTC} = 2.82 \pm 1.16$ t/day and OCC meteoroids $\mathcal{M}_{OCC} = 2.18 \pm 1.16$ t/day. It is critical to note that these values are presented as an illustration because by taking into account the uncertainty range from Carrillo-Sánchez et al. (2016), that is, the JFC-to-LPC ratio value $\sim 6.92^{+14}_{-4.8}$, the LDEX observations are giving uncertainties for the mass influx at Earth larger than the original work of Carrillo-Sánchez et al. (2016).

In summary, in this section we improved our data-model comparison from the results presented in Janches et al. (2018), who calculated normalized M^+ and treated each month separately, and quantified the uncertainty in the mixing of different populations resulting from the model free parameters. We present one general model that reproduces both the LT dependence of M^+ measured by LDEX, as well as its amplitude changes during the duration of the mission, if we introduce a lunar LT dependence (see equation (10)) to the Koschny and Grün (2001) fit. Furthermore, we explored both the mass and velocity dependence in the M^+ calculation, finding that unless we keep the mass related index γ_1 close to unity, we obtain meteoroid population mixing ratios at Earth that are not in agreement with currently published values by Carrillo-Sánchez et al. (2016). Faced with the same problem, Janches et al. (2018) suggested an increase in the velocity dependence of M^+ to $v^{3.5}$ as a possible solution to the discrepancy in their model fits. Our new insight in this paper is that the dependence of M^+ to meteoroid mass is equally uncertain and would influence the retrieved importance of different ratios even more.

4. Modeled Selenocentric and Temporal Variability of Meteoroid Impactors

Because of the geographical limitations of the LADEE orbit, the previous section provides a limited picture of the influence of meteoroid impacts on the formation of the lunar secondary dust ejecta cloud and exosphere. In this section we expand our work to all selenocentric latitudes and LTs, beyond the near equatorial region covered by the LADEE mission. Specifically we will present model predictions for the orbital elements of meteoroids impacting the Moon, their directions and velocities, and their dependence on lunar phase and time of the year. Furthermore, we will provide estimates of the mass flux, impact vaporization flux, and ejecta mass production rates as a function of lunar LT and latitude given in absolute numbers using the results reported by Carrillo-Sánchez et al. (2016) as a calibration value at Earth. Finally, we will describe the velocity distribution for all possible ecliptic latitude directions of meteoroids that will enable surface exposure calculations (e.g., for craters at different lunar latitudes).

For the results in this section we use population mixing values following Carrillo-Sánchez et al. (2016) and the results of the LDEX observations fitting: $\mathcal{M}_{MBA} = 3,700$ kg/day, $\mathcal{M}_{JFC} = 34,600$ kg/day, $\mathcal{M}_{HTC} = 2,820$ kg/day, $\mathcal{M}_{OCC} = 2,180$ kg/day. It is important to note that we use these values because they are the latest published estimates of these quantities. However, they remain a debated quantity as currently they overpredict measurements by sensitive radars, in particular those from JFCs meteoroids (Janches et al., 2017). Nevertheless, the results presented here can be scaled if revised estimates of the population mixing ratios are reported in the future. We assumed a collisional lifetime multiplier of $F_{coll} = 20$ and a SFD/MFD index of $\alpha = 4$. Henceforth, we will refer to this combination of mixing ratios and model parameters as the "preferred solution." However, we will also explore the dependence of the results on different model free parameters: $F_{coll} \in [10, 50]$ and $\alpha \in [3.4, 4.6]$, in order to characterize our confidence interval.

4.1. Orbital Elements, Radiant Distributions, and the Earth to Moon Mass Flux Ratios

Even though the Moon and Earth are, from a Solar System perspective, close neighbors, the distribution of orbital elements of meteoroids impacting these bodies is significantly different. This is exemplified in

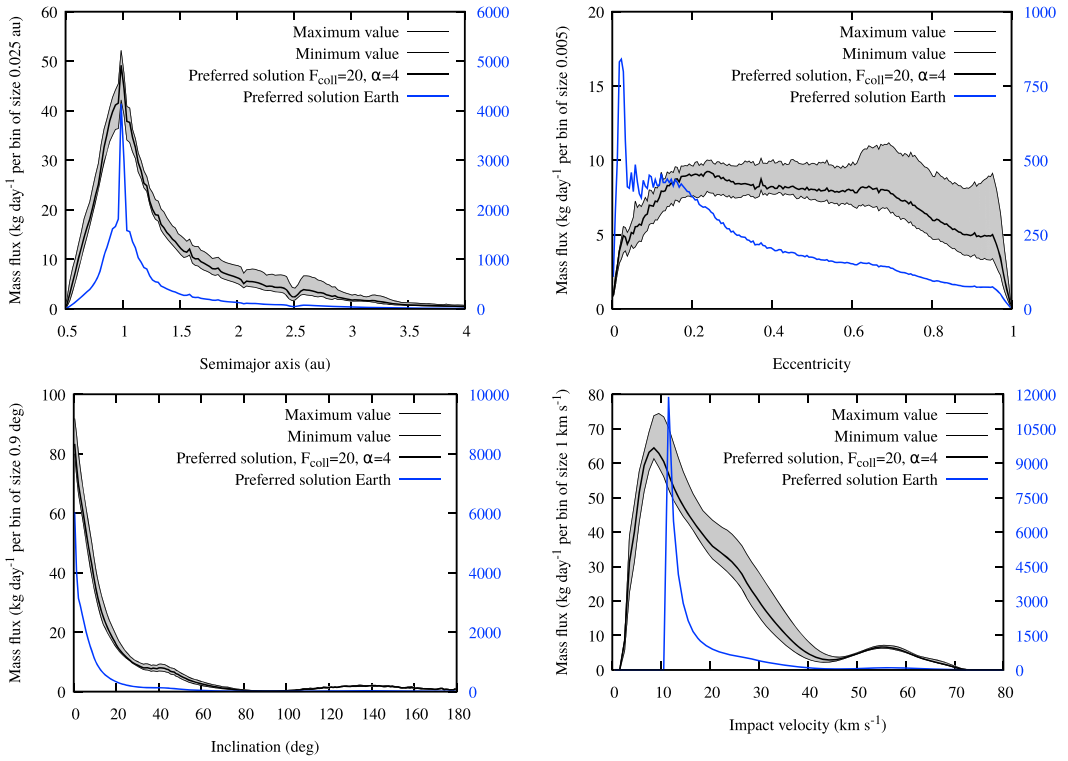

Figure 5. Distribution of orbital elements scaled with the mass flux at Moon (black solid line representing our preferred solution) and at Earth (blue solid line). The gray area is the confidence interval determined from minimum and maximum values for $F_{\mathrm{coll}} \in [10, 50]$ and $\alpha \in [3.4, 4.6]$. Note that the left y axis refers to the mass flux at the Moon while the right y axis in all panels denotes the mass flux at Earth (mass flux at the Moon is always smaller than at Earth).

Figure 5, where semimajor axis a, eccentricity e, inclination i, and impact velocity V_{imp} are shown at both locations, where the Moon is represented by the solid black line and the Earth by the solid blue line. Both curves represent the mass flux averaged over 1 year, where the gray area represents the maximum and minimum values obtained for all possible combinations of free parameters $F_{\mathrm{coll}} \in [10, 50]$ and $\alpha \in [3.4, 4.6]$. Note that the intervals in this figure do not reflect the uncertainty in the mass fluxes for different meteoroid populations reported by Carrillo-Sánchez et al. (2016). The bottom right panel in Figure 5 shows the effect of gravitational focusing at Earth and the Moon. For meteoroids with lower velocities, that is, <30 km/s, the effective collision radius at Earth is significantly larger than that of the Moon. This is due to the larger escape velocity at Earth, $V_{\mathrm{esc}} = 11.2$ km/s as compared to $V_{\mathrm{esc}} = 2.4$ km/s at the Moon (see also equation (3) for reference). This results in a distribution with a sharp peak centered at $V_{\mathrm{imp}} = 11.2$ km/s for the case of Earth, whereas for the Moon the impact velocity distribution is broader, centered at $V_{\mathrm{imp}} = 9$ km/s. Note also the higher fraction of meteoroids with $V_{\mathrm{imp}} > 40$ km/s impacting the Moon, due to the fact that this impact velocity range is much less affected by gravitational focusing. As expected, gravitational focusing also affects other meteoroid orbital elements. The distribution of semimajor axes at Earth has a sharp peak at $a = 1$ au, while it is broader at the Moon with a tail extending beyond 4 au (top left panel in Figure 5). Noticeable dents in the semimajor axis distribution are correlated with the absence of JFC meteoroids around internal mean-motion resonances with Jupiter (e.g., 3:1J at $a = 2.5$ au).

The eccentricity distribution of meteoroids at the Moon is fairly constant for $0.15 < e < 0.8$ (top right panel in Figure 5). The small local peaks close to $e = 1$ are caused by more effective collisions for $F_{\mathrm{coll}} = 10$ preventing larger meteoroids from circularization via PR drag. At Earth, on the other hand, the mass flux exhibits a steady increase with decreasing e with a sharp peak close to $e = 0.005$, again caused by the larger gravitational focusing effect for meteoroids with small relative velocities, since in our preferred solution the meteoroid mass flux at Earth is dominated by JFC meteoroids. Gravitational focusing does not seem to affect the inclination distribution, as can be seen in the bottom left panel of Figure 5, where at both the Earth and the Moon, meteoroid orbits exhibit a peak at $I = 0°$ decreasing rapidly with increasing I to a few percent of

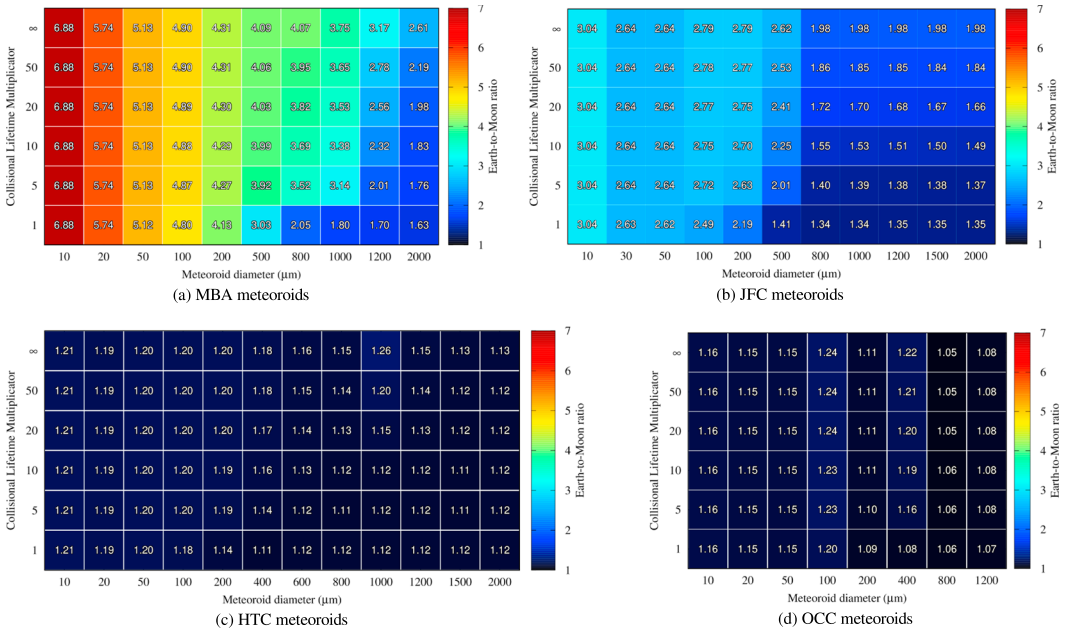

Figure 6. The average Earth-to-Moon mass flux ratio (color coded) with respect to the meteoroid diameter D in micrometer and the collisional lifetime multiplier F_{coll} for meteoroids originating from the MBA, JFCs, HTCs, and OCCs. The mass flux ratio is calculated for a unit area and thus does not take into account different cross-section areas of Earth and Moon. We see that the ratio is the highest for MBA meteoroids that have the lowest relative velocities with respect to the Earth-Moon system. On the other hand, high relative velocities of OCC meteoroids result in a rather small enhancement to the benefit of the Earth. MBA = main-belt asteroid; JFC = Jupiter-Family Comet; HTC = Halley-type comet; OCC = Oort-Cloud Comet.

the peak value for $I \sim 40°$ at Earth and $I \sim 60°$ at Moon. The decrease is sharper at Earth where there are almost no meteoroid orbits with $I = 30°$ while at the Moon, there is a small but noticeable peak centered around $I = 40°$ which is related to the prograde portions of HTC meteoroids. These differences stem from the lower relative velocities of low I meteoroids, which results in a decreased relative contribution of the high I portion of meteoroids impacting the Earth.

From the resulting orbital element distributions it can be concluded that the gravitational focusing (i.e., enhancing the effective radius of the object for passing meteoroids) has a strong effect on the meteoroid orbits at Earth, causing spikes in the impact velocity ($V_{\mathrm{imp}} = 11.2$ km/s), semimajor axis ($a = 1$ au), eccentricity ($e = 0.005$) and inclination ($I = 0°$) (see also for more details Kortenkamp, 2013). Gravitational focusing is much weaker at the Moon leading to a much wider distribution in a, e, I, and V_{imp}. Moreover, gravitational focusing has a significant effect on the total mass flux, where if we assume that Earth accretes $\mathcal{M}_{\mathrm{Earth}} = 43.3$ t/day following Carrillo-Sánchez et al. (2016), the corresponding mass accretion at the Moon equals $\mathcal{M}_{\mathrm{Moon}} = 1.4$ t/day. Since the relative surface ratio between the Earth and the Moon is 13.46, the further decrease of accumulation on the Moon by a factor of three is attributed to gravitational focusing (which affects mostly MBA and JFC meteoroids, as we describe later in the text in more detail). This is in agreement with the initial results presented in Janches et al. (2018) where the contribution of JFC meteoroids at the Moon was found to be similar to that from LPC meteoroids, but about six times lower than the estimates at Earth by Carrillo-Sánchez et al. (2016).

To detail the change of the capture probability by Earth and Moon for all meteoroid diameters D and collisional lifetime multipliers F_{coll}, we constructed the following metric. First, we calculated the collision probability for each meteoroid in our model with Earth every 30.4375 days (365.25/12) for one Earth's orbit and calculated the average collision probability over 1 year per unit cross-section area, which is proportional to the flux. We repeated the same calculation for the Moon, sampling the meteoroid flux in 12-hr intervals, which resulted in 731 temporal slices over 1 year. For both objects we took into account their escape velocities reflecting their gravitational focusing potential through equation (3). Then, we simply divided the flux of meteoroids averaged over 1 year at Earth by that at Moon. The average flux ratio between Earth and Moon

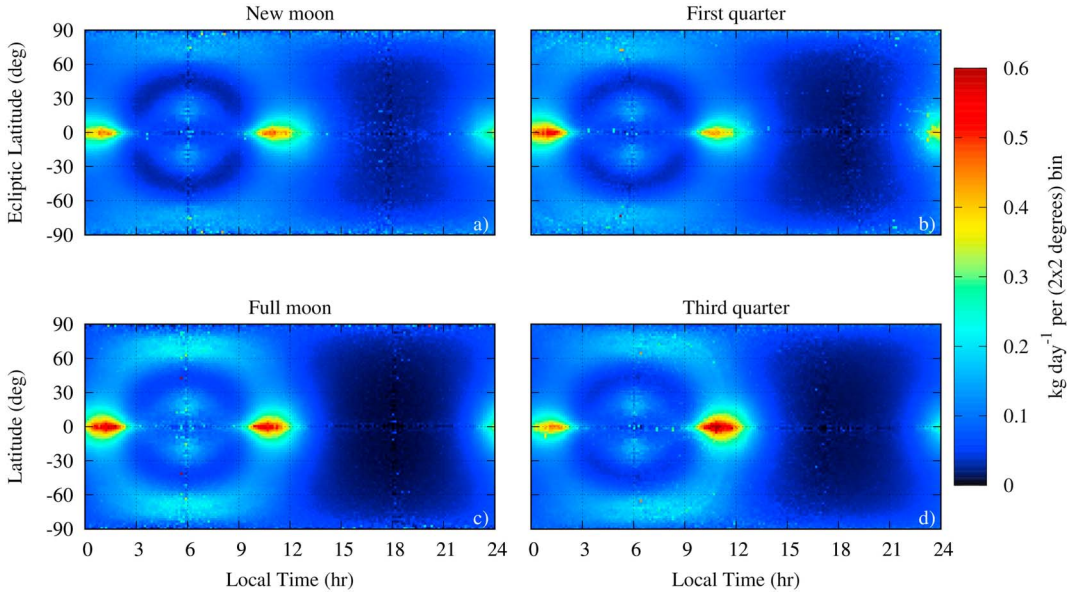

Figure 7. Radiant distribution of meteoroids impacting the Moon for four different lunar phases for the preferred solution during the first lunation in our model (July–August 2013). Different colors represent the mass flux impacting the lunar surface from radiant directions. Units in each of $2 \times 2°$ bins are in kilogram per day. Here, the observer is positioned at the Moon's location, the Moon and Earth are removed, and the whole celestial sphere is visible.

as a function of meteoroid population and diameter is shown in Figure 6. Because of their higher velocities, HTC and OCC meteoroids do not experience significant enhancement of their fluxes at Earth with respect to that at the Moon, the gravitational focusing enhancement is 20–25% at maximum, whereas the slower JFC and MBA grains experience significant enhancement. For all populations the gravitational focusing efficiency decreases with increasing D. For the case of the smallest JFC grains in our model, $D = 10$ μm, the flux is enhanced by a factor of three at Earth when compared to that at the Moon. The gravitational focusing effect is less efficient for $D > 500$ μm, yet an increase of 50–100% is observed even for the largest JFC meteoroids considered in our model. MBA meteoroids show a smooth gradient of the flux ratios caused by more effective trapping of MBA meteoroids in external mean-motion resonances with Earth that is increasing their eccentricity and consequently the impact velocity. For larger MBA grains there is an effect of collisions, which is an amalgam of several effects: (1) the timescale of PR drag is longer for larger D, (2) consequently meteoroids can spend more time in mean-motion and secular resonances, and (3) larger meteoroids for the same reason spend more time in planet crossing orbits. All these effects make circularization by PR drag less efficient with increasing D. Longer PR timescales also increase the probability of collision with the Zodiacal cloud, which is apparent in an increased ratio for longer collisional lifetimes, $F_{\mathrm{coll}} > 20$.

Figure 7 shows the radiant distribution of meteoroids impacting the Moon for four different Moon phases during the first lunation in our model (July–August 2013). The predicted radiant distributions are similar to what different radar and optical facilities observe at Earth (e.g., Campbell-Brown, 2008; Janches et al., 2015; Jenniskens et al., 2016). The x axis in Figure 7 is the LT at the Moon. Thus, 0 hr refers to meteoroids impacting from the opposite direction of the Sun (antihelion source, AH), 6 hr is the apex (AP) of Earth's motion, 12 hr represents meteoroids coming from the direction of the Sun (helion source, HE), and 18 hr is the anti-apex (anti-AP). We do not use lunar apex as the reference point, since it significantly changes, unlike Earth's apex that is always perpendicular to the subsolar point. The y axis here is the ecliptic latitude. The ecliptic latitude is almost interchangeable with the selenographic latitude, with only small corrections due to a small axial tilt of the Moon with respect to the ecliptic; ~1.5°. During the new moon phase (Figure 7a) the lunar velocity vector points toward the anti-apex source leading to an enhancement of impacts around 18 hr, while the HE and AH sources are symmetric. During the first quarter phase and up to full Moon, the Moon is moving away from the Sun toward the antihelion source, which increases the abundance of impacts in the nightside (Figure 7b). The apex source is enhanced during the full moon (Figure 7c) because the lunar and Earth's velocity vector are aligned. The third quarter phase is antisymmetric with respect to the first quarter phase, resulting in the enhanced dayside/helion source (Figure 7d). Monthly mass flux

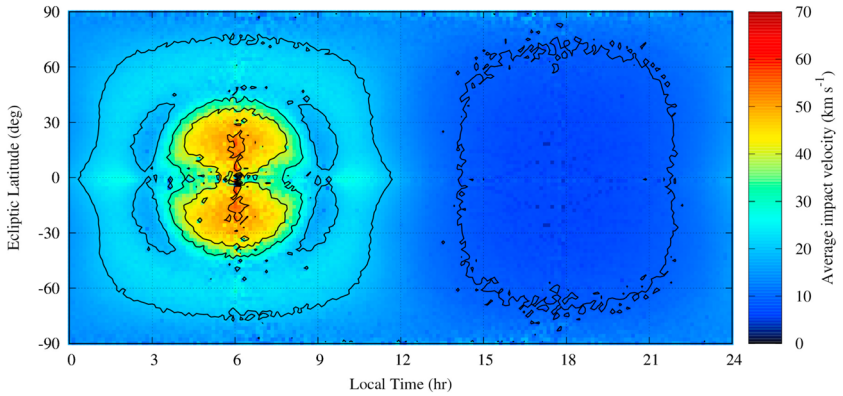

Figure 8. Average impact velocity of meteoroids impacting the Moon from different radiant locations for the preferred solution. Average impact velocity is calculated over the entire year in order to avoid monthly and yearly variations. The contours (black solid lines) represent 10 km/s increments in the average impact velocity. Here, the observer is positioned at the Moon's location, the Moon and Earth are removed, and the whole celestial sphere is visible.

variations are additionally enhanced by yearly variations caused by the motion of the Earth, where, due to the Earth's small eccentricity ($e = 0.0167$), the overall flux is smallest at aphelion (early July) and largest at perihelion (early January). There is also a subtle enhancement of the helion source when Earth is moving from aphelion to perihelion with maximum at autumnal equinox (September), and a symmetric effect at vernal equinox (March) for the antihelion source. These changes are not easy to recognize in the radiant distributions plots but will be shown in the following Section.

4.2. Velocity Distributions and Latitudinal Profile of Lunar Meteoroid Impactors

Figure 8 displays the average impact velocity of meteoroids impacting the Moon's surface as a function of LT and ecliptic latitude (i.e., radiant direction). Given Earth's almost circular orbit and the relatively small orbital velocity of the Moon (~1 km/s) with respect to most impacting meteoroids, this quantity is nearly constant throughout the year. The average impact velocity for most directions is greater than 25 km/s and any changes can be expected only around the anti-apex direction (18 hr). The overall distribution is very similar to that observed at Earth (see, e.g., Figure 16 in Campbell-Brown, 2008), with the apex source populated by retrograde HTC and OCC meteoroids having the highest average impact velocity $V_{\mathrm{imp}} \sim 55$ km/s, followed by the helion/antihelion sources with $V_{\mathrm{imp}} \sim 30$ km/s, and the toroidal/ring structure with $V_{\mathrm{imp}} \sim 25$ km/s. Note that even meteoroids with radiants at the highest ecliptic latitudes (i.e., meteoroids impacting the lunar poles from zenith) have considerable average impact velocities ($V_{\mathrm{imp}} \sim 15$ km/s), which implies the possibility of highly energetic impacts in all craters on both lunar poles.

To show more clearly the full distribution of impactor speed as a function of latitude, we calculated an average mass flux over one lunation between 7 July 2013 and 6 August 2013 in the ecliptic latitude and impact velocity space (Figure 9). Figure 9 shows the mass flux distribution for all ecliptic latitudes and impact velocities per 2° and 2 km/s bins. Because in spherical coordinates the surface area derivative is $\propto \cos(\beta)$, a correction $[1/\cos(\beta)]$ must be applied in order to calculate the mass flux per unit area. We readily see that the whole lunar surface is exposed to impacts with V_{imp} up to 30 km/s, where the highest velocity impacts originate from HTC and OCC meteoroids. We also note that the impact velocity generally decreases with the ecliptic latitude of meteoroids.

It is evident from these last two figures that meteoroids reach the polar regions. The access of meteoroids to permanently shadowed craters near the lunar poles is of special interest and will be the subject of a future study with our model. As an initial approach we assume here a crater at the selenocentric latitude Θ_{Moon} and the minimum incidence angle θ measured from the vertical (i.e., 0° represents impacts from the zenith). Then in order to reach the floor of such a crater, a given impactor must have the ecliptic latitude β:

$$\Theta_{\mathrm{Moon}} - \theta \leq \beta \leq \Theta_{\mathrm{Moon}} + \theta, \tag{11}$$

Equation (11) assumes that the impacted object has no axial tilt with respect to the ecliptic, which is an acceptable simplification for the Moon. Let us use Shackleton crater as an example with $\Theta_{\mathrm{Moon}} = -89°$, that

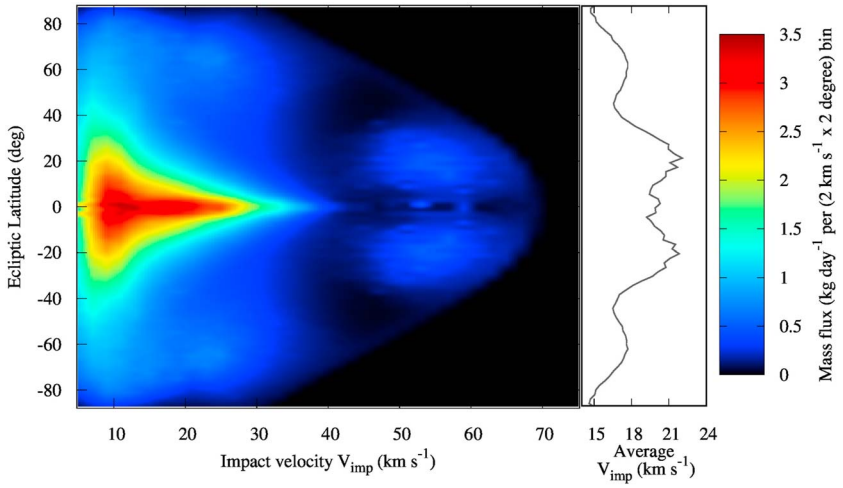

Figure 9. Distribution of mass fluxes for meteoroid impact velocities V_{imp} with respect to the entire range of ecliptic latitudes β. Although data shown here reflect the model for 7 July 2013, the overall distribution does not significantly change during the year. The gray line on the left hand side shows the average meteoroid impact velocity for each ecliptic latitude.

has a reported highest local-slope ~25°, which translates to $\theta = 65°$ (Zuber et al., 2012). Then, the range of ecliptic latitudes for meteoroids that can impact the floor of Shackleton crater would be $-90° \leq \beta < -24°$. This means that based on results in Figure 9, the Shackleton impact crater is accessible for meteoroids even with velocities $V_{\text{imp}} > 40$ km/s.

4.3. Temporal Variability of the Micrometeoroid Mass Flux Accreted by the Moon

The flux of meteoroids impacting the Moon varies over two timescales. Monthly variations are due to changes in the orbital velocity of the Moon around the Earth, and yearly variations are due to changes in the heliocentric distance of Earth that follows from the nonzero eccentricity of its orbit. The magnitude of these two effects is quantified in Figure 10, which shows the total mass flux on the Moon over one Earth year. In this figure the solid black line represents the preferred solution, the gray shaded area contains the

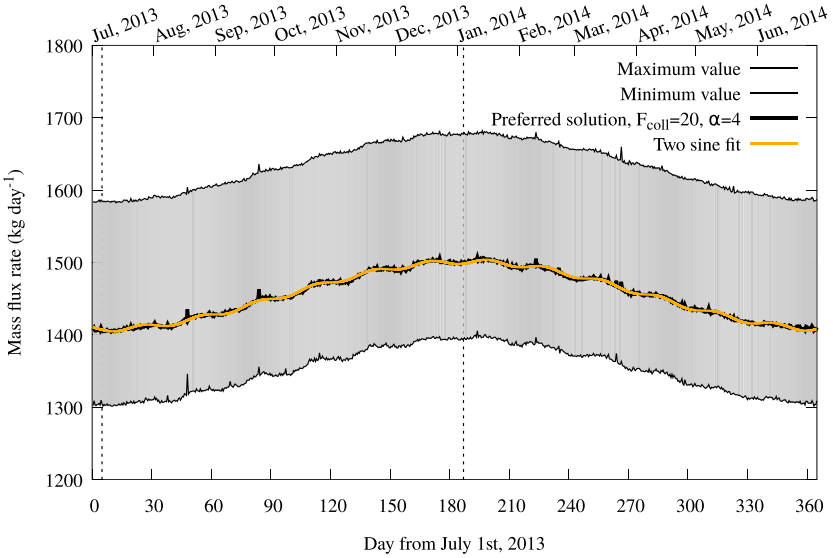

Figure 10. Variations of the mass flux rate in kilogram per day with time from 1 July 2013 to 30 June 2014. The preferred solution for our model is represented by a thick black solid line, while the confidence interval is shown as the gray area between two black solid curves denoting minimum and maximum variations of the model. The orange thick line is a fit to our preferred solution by a sum of two sines (equation (12)). Two dashed vertical lines represent the time of aphelion (5 July 2013) and perihelion (4 January 2014) passage.

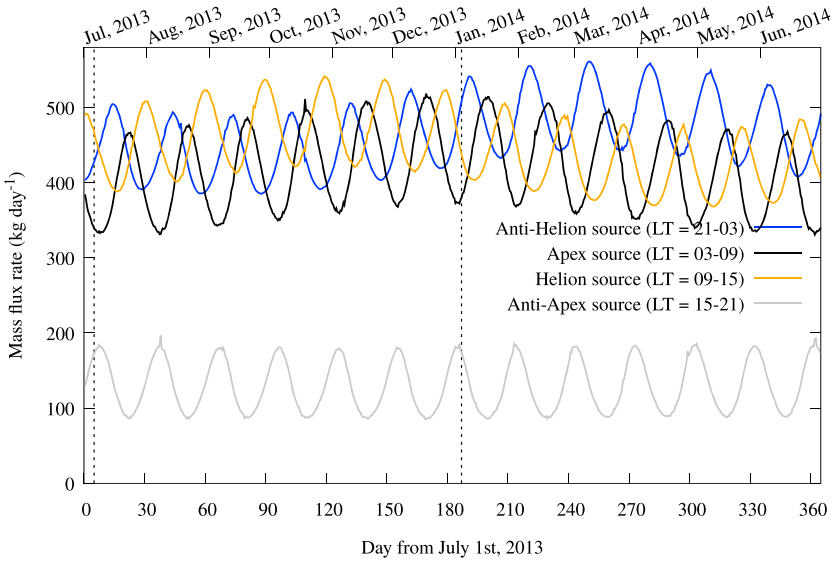

Figure 11. The same as in Figure 10, but now our preferred solution is divided to four distinctive sources/uniform segments in local time. The blue solid line represents the antihelion source (LT = 21–03 hr), black solid line the apex source (LT = 03–09 hr), orange solid line the helion source (LT = 09–15), and the anti-apex source is represented by the gray solid line. Notice that the variations of antihelion and helion sources are anticorrelated, which is a consequence of the direction change of the orbital velocity vector of the Moon around the Earth. Two dashed vertical lines represent the time of aphelion (5 July 2013) and perihelion (4 January 2014) passage.

solutions for F_{coll} and α values in the range of 10–50 and 3.4–4.6, respectively, and the orange solid line is an analytical fit of the preferred solution which is obtained using the following function:

$$f(t) = a_1 \sin(t/P_1 + t_1) + a_2 \sin(x/P_2 + t_2) + M_0, \tag{12}$$

where t is time in days and $a_1 = -46.5861, P_1 = 58.6734, t_1 = 1.4710, a_2 = -2.6956, P_2 = 4.6410, t_2 = -0.5900, M_0 = 1385.7252$ are fitting constants. Readily, we recognize that M_0 represents the average mass flux per year, a_1 and a_2 are yearly and monthly amplitudes, respectively, $P_1 \sim 365.25/2\pi$ and $P_2 \sim 29.5/2\pi$ are related to orbital periods of the Earth and synodic period of the Moon, respectively, and t_1, t_2 are temporal offsets of our fit. The yearly variations amount to 3.3% of the average mass flux, while the monthly variations amount to 0.2%. These numbers represent variations of the total flux of all meteoroids from each direction every day, but, as we showed in Figure 7, there is a noticeable difference of mass flux between the dayside and nightside sources. From Figure 10 we see that the confidence area is quite wide and our preferred solution is closer to the minimum value of this interval. This is a direct consequence of the different magnitudes of gravitational focusing effect for different collisional lifetimes and SFDs (see Figure 6). The minimum values shown in Figure 10 represent model results with $\alpha = 4.6$, while maximum values are referring to solutions with $\alpha = 3.4$. The effect of varying F_{coll} is an order of magnitude smaller than those obtained by varying α. Notice that the overall shape of the mass flux variations for different representations of our model does not change.

Figure 11 shows variations of the mass flux at the Moon for four different lunar LT periods. Each one of these periods will be dominated by a particular meteoroid population: the antihelion (AH; blue solid line; 21–03 hr), helion (HE; orange solid line; 09–15 hr) and apex (AP; black solid line; 03–09 hr) sources have similar strengths throughout the year and experience significant monthly and yearly variations. The anti-apex source (gray solid line; 15–21 hr) is 3.3 times weaker than the apex source and has negligible yearly variations. Using equation (12) once again to fit the curves in Figure 11, independently, results in helion (HE) and antihelion (AH) sources with similar yearly means: $M_{0_{\mathrm{HE}}} = 420$ kg/day, $M_{0_{\mathrm{AH}}} = 438$ kg/day, and a slightly smaller apex source yearly mean: $M_{0_{\mathrm{AP}}} = 406$ kg/day. Yearly amplitudes are approximately 7.5% for the HE/AH sources, and 6.2% for the apex source. The monthly variations of the AH/HE sources are approximately 12%, while the apex source has slightly higher amplitudes, ~16%. Note that the HE/AH sources monthly variations are anticorrelated in time so the dayside/nightside asymmetry is even larger. The

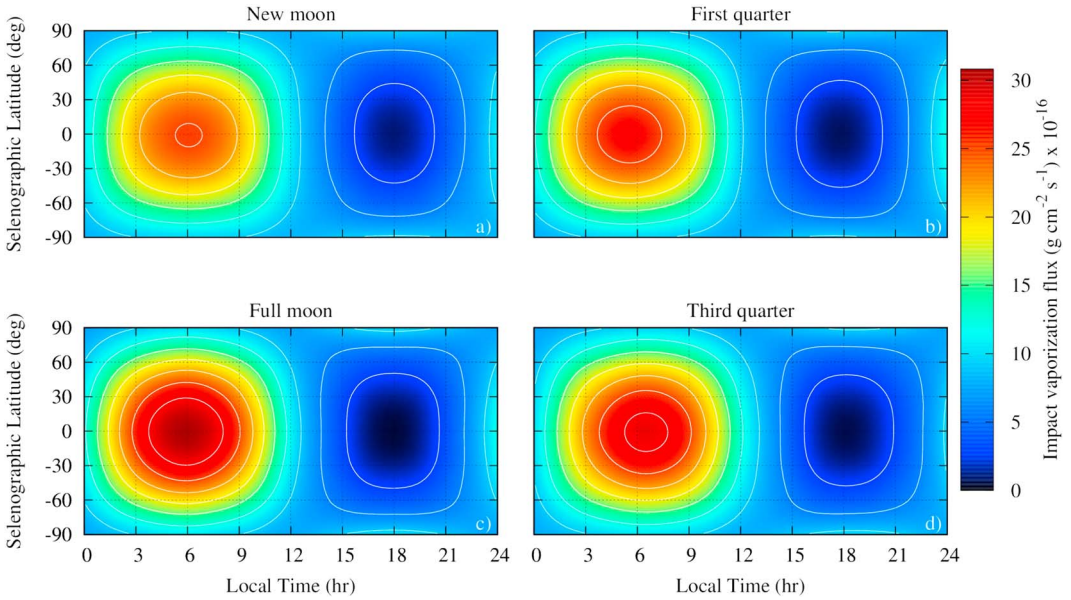

Figure 12. Impact vaporization flux (color coded) for our preferred solution for four lunar phases for the first lunation in our model during 7 July and 6 August 2013. The x axis shows the local time on the lunar surface, where 12 hr is the subsolar point. The y axis is the selenocentric latitude in degrees. The contours (white solid lines) represent 10% increments from 0 to the maximum value. Units of the impact vaporization flux are g·cm^{-2}·s^{-1} ×10^{-16}.

anti-apex experiences the highest relative monthly variations of 37% due to small impact velocities of meteoroids in this source and thus higher relative changes caused by Moon's orbital velocity. The HE and AH sources are offset by 183 days, where the HE source has the yearly maximum during the autumnal equinox, and the AH source then peaks during the vernal equinox, which confirms the results reported in Janches et al. (2018).

5. Meteoroid Impact Effects on the Lunar Surface

Knowing the distributions of directions, velocities, and masses of meteoroids at any given time allows us to predict measurables of various processes that take place on the lunar surface, in particular to model the dust ejecta cloud surrounding the Moon or the impact vaporization flux at the lunar surface. Each combination of the meteoroid direction, velocity, and mass in our model (referred as the Lunar Meteor Input Function; Janches et al., 2018) represents a stream of meteoroids with common properties impacting one hemisphere of the lunar surface. First we convert the meteoroid flux from steradians (Figure 7) to the mass flux from an apparent zenith per unit area by applying a factor $1/\cos(\beta)$, where β is the meteoroid ecliptic latitude and which accounts for the smaller surface area of elements at higher latitudes. The resulting zenith flux $\mathcal{Z}$ allows us to calculate the flux to each surface element. We assume that the meteoroid flux decreases as $\cos(\mathcal{A})$, where $\mathcal{A}$ is the angular distance from the zenith for a particular surface element. For $\mathcal{A} > 90°$ the meteoroid flux is always 0. The zenith flux $\mathcal{Z}$ does not diverge at the poles in our model since the probability of $\beta = \pm 90$ is 0. With the meteoroid flux per surface area we incorporate the impactor velocity and using equations 6 and 8, we calculate the absolute impact vaporization flux and ejecta mass production rate for each lunar surface element in our model (16,200 spherical elements, corresponding to steps of 2° in selenographic latitude and 8 min in lunar LT).

5.1. Meteoroid Impact Vaporization

First, we study the LT dependence of the impact vaporization source of neutrals for the lunar exosphere. The resulting impact vaporization flux $\mathcal{F}$ (see equation 6) from the lunar surface is shown in Figure 12, where the colors represent the absolute impact vaporization flux $\mathcal{F}$ in grams per centimeter squared per second times ten to minus sixteen, shown for one lunation from 7 July to 6 August 2013. Note that these values result from assuming the "preferred solution" described in the previous sections. For this combination of meteoroid sources only a slight motion of the peak is expected within a month. The contours in Figure 12 show a hotspot centered at dawn (6 hr of LT) during the new moon phase having a peak value $\mathcal{F} = 24.36$ g·cm^{-2}·s^{-1} × 10^{-16},

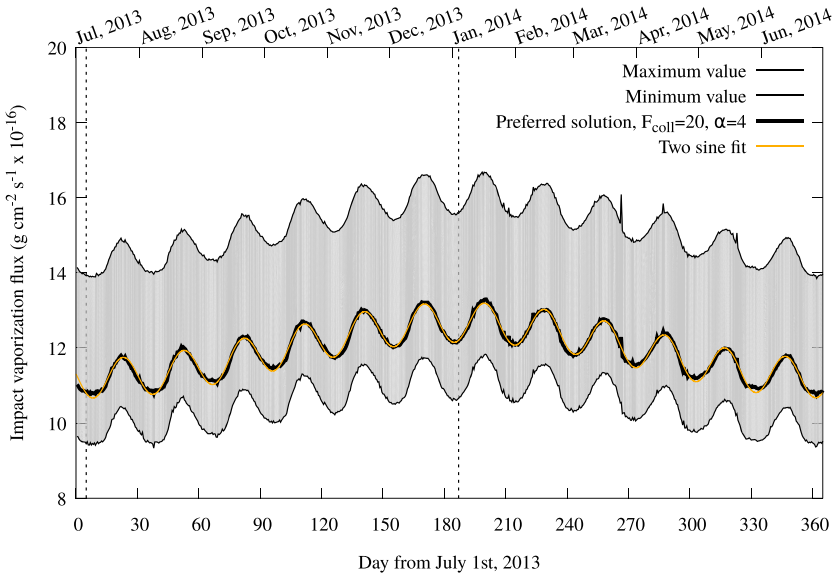

Figure 13. Variations of the impact vaporization flux rate in g·cm^{-2}·s^{-1} × 10^{-16}. with time from 1 July 2013 to 30 June 2014. The preferred solution for our model is represented by a thick black solid line, while the confidence interval is shown as the gray area between two black solid curves denoting minimum and maximum variations of the model. The orange thick line is a fit to our preferred solution by a sum of two sines (equation 12). Two dashed vertical lines represent the time of aphelion (5 July 2013) and perihelion (4 January 2014) passage.

which represents 81% of the full moon phase values. During the first quarter phase, and as the Moon is moving away from the Sun, the center of the hotspot shifts slightly to the nightside peaking at LT = 5:30 hr, and with a relatively small increased maximum impact vaporization flux, $\mathcal{F} = 25.80$ g·cm^{-2}·s^{-1} × 10^{-16}. During the full moon phase the impact vaporization flux is close to the maximum for a particular lunation, $\mathcal{F} = 30.05$ g·cm^{-2}·s^{-1} × 10^{-16}, and the peak shifts back to the dawn terminator. Since the Earth is moving toward perihelion the dayside/helion source is slightly stronger than the nightside/antihelion source during the first quarter. The impact vaporization rates follow the same trend as the mass flux variations shown in Figure 11. During the third quarter the maximum impact vaporization flux is $\mathcal{F} = 28.01$ g·cm^{-2}·s^{-1} × 10^{-16} with the peak value shifted to LT = 6:28 hr. The actual maximum value of $\mathcal{F}$ during this lunation occurs 2 days after the full moon phase.

From Figure 11 we concluded that variations of the mass flux on scales of 20% are expected over a period of a month for different LTs. Variations of the impact vaporization flux $\mathcal{F}$ during the entire year are shown in Figure 13, where we show the preferred solution (black solid line, $F_{\text{coll}} = 20, \alpha = 4$ and the population mixing derived in section 3) and the confidence interval calculated as the minimum and maximum values for all combinations of $F_{\text{coll}} \in [10, 50]$ and $\alpha \in [3.4, 4.6]$. Note that the confidence interval does not reflect the uncertainty of abundances of different meteoroid populations in Carrillo-Sánchez et al. (2016). Using equation (12) the best fit to the preferred solution results in the following fitting constants: $a_1 = -0.7412, P_1 = 57.3646, t_1 = 1.4311, a_2 = -0.5276, P_2 = 4.6839, t_2 = -0.2020, M_0 = 11.9362$, where units for $a_1, a_2,$ andM_0 are g·cm^{-2}·s^{-1} × 10^{-16}. Over a period of a year, the expected variations of the impact vaporization flux are of the order of 6–8% for any model in our confidence interval and the total monthly variations are of the order of 4–5%. As shown for the Hermean meteoroid environment (Pokorný et al., 2018) and as previously suggested at the Moon (Szalay & Horányi, 2015), meteoroids from the apex source (i.e., retrograde HTCs and OCCs meteoroids) dominate the total impact vaporization flux due to its higher impact velocities because $\mathcal{F} \propto V_{\text{imp}}^2$. The monthly variability of the apex source is further enhanced due to the fact that the antihelion/helion variations are anticorrelated and thus their sum is effectively suppressing monthly variations. Fitting the individual sources similarly done for the mass flux (Figure 11) results in relative contributions of the apex, helion/antihelion, and anti-apex sources of the order of ~56%, ~21%, and 2% of the total impact vaporization flux, respectively.

Similar to previous calculations (e.g., Bruno et al., 2007; Cremonese et al., 2013), our model confirms that impact vaporization is an important source of neutrals for the lunar exosphere. In particular, the peak pro-

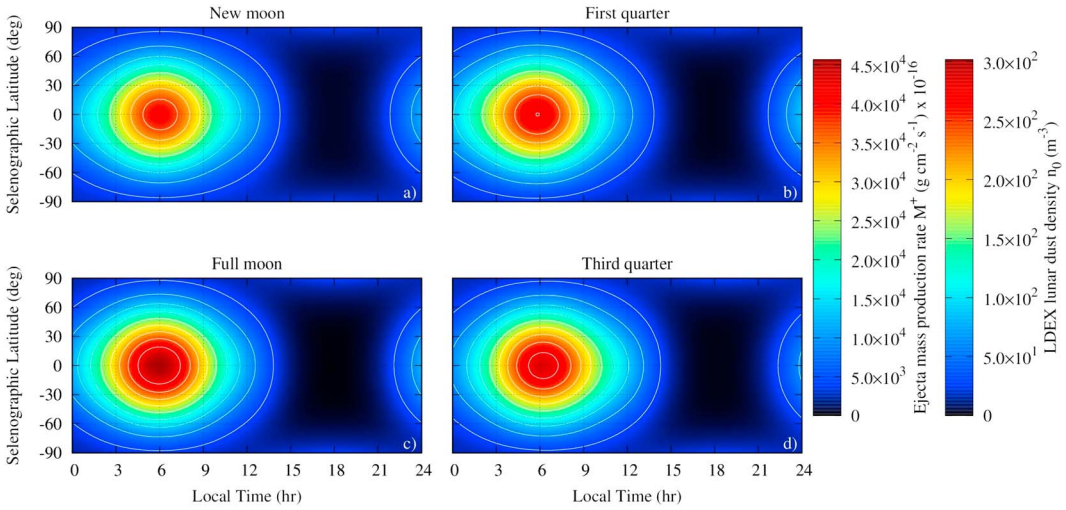

Figure 14. The ejecta mass production rate M^+ (color coded with the range of values represented by the left color box) for the first lunation (four moon phases) in our model in July and August 2013. The x axis is the local time in hours and the y axis is the selenographic latitude in degrees. The second color box represents n_0, the LDEX lunar dust density (units of m^{-3}) for an average particle radius of $r_{LDEX} = 0.3\mu$m. LDEX = Lunar Dust Experiment.

duction of Na vapor at dawn over the one lunation shown in Figure 12 is estimated to be 1.5×10^5 cm^{-2}/s if the fraction of sodium in the soil is assumed to be 0.0031 (Wurz et al., 2007). This is about one tenth of the inferred photodesorption flux of 2×10^6 cm^{-2}/s required to sustain the observed lunar Na brightness at noon (Sarantos et al., 2010). However, the meteoroid impact vaporization, rather than sputtering, is likely the dominant source of the original sodium atoms from minerals and rocks. Our global-averaged vapor calculations, 11.6×10^{-16} g·cm^{-2}·s^{-1}, are a factor of ~6 higher than the total vapor flux assumed by Sarantos et al. (2012), 1.78×10^{-16} g·cm^{-2}·s^{-1}, implying that impacts should produce a brighter than previously estimated exosphere for all lunar metals.

The assertion that most of the vapor is produced by apex impactors assumes no velocity-dependent losses to other processes (ionization, oxide, and condensate formation) in the impact vapor. Using a similar model calibration to that used here, Pokorný et al. (2018) found that the amount of predicted impact vaporization flux on Mercury's surface is two orders of magnitude larger for species such as Mg than the estimated values derived from the *MErcury Surface, Space ENvironment, GEochemstry, and Ranging (MESSENGER)* spacecraft observations (Merkel et al., 2017). In order to find agreement between the dynamical meteoroid model and the observations, the authors suggested that the impact vaporization relation (equation (6)) may overestimate the contribution of higher impact velocities $V_{imp} > 20$ km/s to the total vapor because of losses to other phases (Berezhnoy, 2013). If that is the case, both the total impact vaporization rates and the LT dependence of the impact-derived exosphere will be different. When excluding all high velocity impactors ($V_{imp} < 20$ km/s) our model predicts a considerable variation impact vaporization flux in LT every month. The apex source no longer dominates the impact vaporization flux and is replaced by then dominating the midnight/noon sources.

5.2. Ejecta Mass Production Rates and Gardening of the Lunar Surface

In section 3 we focused on the ejecta mass production rates of meteoroid impacts as observed by the LDEX instrument onboard LADEE, which provided coverage limited to selenographic latitudes $-23° < \Theta_{Moon} < 24°$. Figure 14 shows the lunar ejecta production rate in a broader set of LTs and latitudes during four lunar phases from 7 July to 6 August 2013. The rates were calculated using equation (8), in which $C = 3.067 \times 10^{-7}$m$^{-2.46}$ s$^{2.46} = 7.358$km$^{-2.46}$ s$^{2.46}$ was rederived using data from Koschny and Grün (2001) with $\gamma_1 = 1, \gamma_2 = 1.23$ (see equation (8)). Since $\mathcal{F}$ and M^+ have a similar proportionality to energy of the impacting meteoroid, results for these two quantities are not at first glance significantly different, except for differences stemming from the angular scaling.

The $\cos^3(\mathcal{A})$ scaling (the additional power of cosine comes from the surface patch projection) produces a sharper gradient from the apex source, which is more apparent from contours in Figure 14. Between 15 and

21 hr of lunar LT and $-45° < \Theta_{\text{Moon}} < 45°$ M^+ is almost zero. This effect persists for all possible combinations of free parameters in our model and reflects the reduced access of meteoroids to dusk regions. The largest concentration of mass production rates is expected at dawn due to the dominance of ejecta yield by the high velocities of apex meteoroids, while the helion/antihelion variations within the month cause only small changes in the overall map of lunar ejecta mass production rates. We also see that the polar regions show considerable ejecta mass production at all LTs.

Comparison of absolute values of $\mathcal{F}$ and M^+ shows that M^+ is three orders of magnitude larger than $\mathcal{F}$. The reason for that stems from the coefficient values in equations 6 and 8, where the ejecta-to-vaporization ratio $C/e = 7.357/0.0604 = 121.8$. Additionally, the stronger dependence of M^+ on the impact velocity further increases the difference between $\mathcal{F}$ and M^+. Using the minimum detected particle radius by LDEX $r_{\text{LDEX}} = 0.3\mu$m and average lunar ejecta velocity $\bar{v} = 670$ m/s (Szalay & Horányi, 2016) we can convert M^+ to the lunar dust density n_0 as observed by LDEX:

$$n_0 = \frac{M^+}{\frac{4}{3}\pi r_{\text{LDEX}}^3 \rho_{\text{ejecta}} \bar{v}}, \tag{13}$$

where ρ_{ejecta} is the ejecta density. Our model predicts the lunar dust density measured by LDEX n_0 (second color bar in Figure 14) to be four to five orders of magnitude higher than values reported by Horányi et al. (2015) and Szalay and Horányi (2016). In order to obtain lunar dust densities in agreement with those observed by LDEX, the detector would have to miss 99.9975% of all ejecta. Should the average ejecta size be much larger than previously thought, r_{LDEX} would need to be increased to 10 μm, that is, the average ejecta mass needs to be increased by a factor of 40,000. Another way to view this result is to calculate a depth accumulation rate $\delta = M^+/\rho_{\text{ejecta}}$, which represents the cumulative depth of the surface material lifted from the lunar surface over a period of time. Averaged over the equatorial area our model predicts that $\delta_{\text{eq}} = 23$ cm/Myr are excavated by small meteoroids, and averaged over the entire lunar surface $\delta_{\text{eq}} = 14$ cm/Myr. Such values, while orders of magnitude larger than results determined from LADEE measurements (Szalay & Horányi, 2016), are within the same order of magnitude as in situ reworking depths determined from Apollo missions ($\delta_{\text{APOLLO}} = 2.2$ cm/Myr; Morris, 1978) and only one order of magnitude larger than the recent update to the regolith mixing model by Costello et al. (2018), who calculated the soil reworking rates from meteoroids to be $\delta \leq 1$ cm/Myr assuming impactors with $V = 20$ km/s.

Possible causes for this large disagreement between our model and LDEX observations are the following: (1) our model predictions are sensitive to coefficients γ_1, γ_2 in equation (8), (2) the yield of meteoroid impacts on the lunar regolith is much smaller than values derived from the Koschny and Grün (2001) experiment, and (3) LDEX is able to observe only a small fraction of the lunar dust density n_0. With respect to (1), we tested the sensitivity to coefficients from equation (8), $\gamma_1 \in [1.0, 1.3]$ and $\gamma_2 \in [1.0, 1.3]$, where we recalculated C using Koschny and Grün (2001) experimental data. In summary, all possible combinations of γ_1 and γ_2 result in at most 50% differences with respect to the values in Figure 14. With regard to (2), hypervelocity impact experiments with lunar regolith or a similar substrate conducted in microgravity have never been performed, and thus no data regarding the mass ejecta production rates in this environment exist. Finally, investigating (3) would require an in-depth reanalysis of all LDEX detectability calculations and biases that is beyond the scope of this manuscript.

6. Model Limitations

In this work we presented a dynamical model constructed when we combine different sources of meteoroids in the solar system using a selected SFD, collisional lifetime multiplier, and population mixing at Earth. Since various ground-based and space-borne observations of the current meteoroid environment around 1 au can be sufficiently described by the four meteoroid generating populations modeled here (MBAs, JFCs, HTCs, and OCCs), we do not expect a new source of meteoroids producing an abundant signal at 1 au to be discovered in the near future. And although meteoroids originating in the Kuiper belt are a possibly significant population in the outer solar system, Poppe (2016) and Kuchner and Stark (2010) showed that Kuiper-belt meteoroids are unlikely to reach orbits with heliocentric distances below 5 au due to an effective barrier posed by Jupiter.

Our choice for the collisional lifetime multiplier F_{coll} follows results reported by Nesvorný, Janches, et al. (2011) and Pokorný et al. (2014), who suggested that $F_{coll} < 10$ would produce a meteoroid environment for JFC and HTC meteoroids that cannot reproduce the observed distributions of meteors at Earth. We recognize that using F_{coll} as a scale factor is rather a choice driven by necessity and that a full-fledged collisional model derived from first principles is needed to fully resolve this issue. Moreover, we assume F_{coll} is the same for all meteoroid populations, while it is likely that fluffy cometary particles react differently to mutual collisions with the Zodiacal cloud than compact asteroidal meteoroids. Grun et al. (1985) provided more complex conditions for catastrophic destruction in particle-particle collisions involving the particle compressive strength, kinetic energy, and particle mass (see equations 12–15 in Grun et al., 1985). Such implementation would require a priori knowledge of the particle material characteristics and a thorough reanalysis of all dynamical models included in this manuscript to check how the new approach is able to fit available constraints. Even though it is difficult to predict how changes in the collisional grooming methods would change the results of this paper, it is encouraging to note that, as shown in section 3, variations of F_{coll} have an order of magnitude smaller effect on the ejecta mass production rate than variations of the assumed SFD, and currently the lunar observations such as LDEX are limited in constraining these important quantities. Furthermore, our analysis shows that for $F_{coll} > 50$ collisions play a minor role for almost all meteoroid sizes except for $D > 1{,}000$ μm.

Our selection of the preferred SFD range at the source of the various meteoroid populations, $\alpha = [3.4, 4.6]$, is driven by current observations of this quantity at Earth, and individual in situ observations of comets (see section 2.4 for discussion). In section 3 we showed that the SFD changes the meteoroid population mixing required to reproduce LDEX observations, while Pokorný et al. (2014) showed that HTC meteoroids could fit the radar observations of sporadic toroidal meteors for a wide range of SFDs. Nesvorný, Janches, et al. (2011) showed that for various SFDs it is possible to model both the meteor distributions at Earth, meteoroid flux at low Earth orbit, and the latitudinal profile of the Zodiacal cloud. Our selection of SFD is further supported by the recent study of Yang et al. (2018), who suggest similar values of α for the range of diameters of meteoroids considered in the model presented here. We also simplified our selection of SFD such that we use the same SFD for all populations in this manuscript. It would be a rather fortuitous coincidence if all distinctive meteoroid populations had similar SFDs. Investigation of more complex SFD functions and selecting proper SFDs for individual meteoroid populations is left for future work when more observations are available.

While the free parameters discussed above change the overall shape of the meteoroid environment at 1 au, the uncertainty of the absolute calibration of our model is mostly dominated by uncertainties from Carrillo-Sánchez et al. (2016), whose results suffer from similar ambiguity of contributions from different meteoroid population as does our LDEX calibration. Since Carrillo-Sánchez et al. (2016) aimed to simultaneously reproduce lidar observations of the vertical Na and Fe fluxes above 87.5 km and the measured cosmic spherule accretion rate at the South Pole, it is understandable that different meteoroid populations, despite having different compositions, cannot be disentangled by a single observation. Using the mass flux at Earth as one of our constraints helps us to place limits all processes at the Moon that linearly scale with the mass flux, that is, the mass flux on the lunar surface, the impact vaporization rate and, to some degree, the ejecta mass production rate. Processes that strongly depend on the SFD, such as the lunar dust cloud density or the number of meteoroids impacting the lunar surface, are rather poorly constrained due to the power law nature of the SFD.

Cremonese et al. (2012) reinvestigated the *LDEF* spacecraft impact measurements with a different terrestrial mass flux calibration than used here, with $M_{JFC} = 11.5 \pm 1.4$ t/day, and $M_{MBA} = 20.3 \pm 2.8$ t/day. These values were later used in Cremonese et al. (2013) and Borin et al. (2017) to estimate the meteoroid flux at the Moon. The calibration for LPCs was not provided in these works so for the sake of direct comparison we assume that HTC and OCC contribution is the same as in the calibration presented in this manuscript. This would lead to the following lunar mass influx: $M_{Moon_{JFC}} = 0.34 \pm 0.04$ t/day, and $M_{Moon_{MBA}} = 0.35 \pm 0.05$ t/day, which is approximately three times smaller lunar mass flux for JFCs and five times larger for MBA than our model calibration. This would lead to a suppression of the importance of $V_{imp} < 30$ km/s impacts coming from $\pm 30°$ range in the ecliptic latitude, and would shift the velocity distribution to smaller impact velocities (from ~9 to ~6.5 km/s). The effect on the impact vaporization and ejecta mass production rates resulting from the alternative calculation would be rather small. Due to the fact that both of these quantities are dominated by the contribution from LPC meteoroids, a decrease in the overall mass flux of slower meteoroid populations and a shift to smaller impact velocities would result in diminishing the importance of both JFC

and MBA contributions. However, resolving the discrepancy between our model and LDEX measurements would require orders of magnitude smaller mass flux from all populations assumed here. Should we remove the contribution of LPC meteoroids completely from the inner solar system, MBA and JFC meteoroids would not be able to create the dust cloud profile observed by LDEX near the dawn terminator (LT = 06–07; see Figure 3).

Interpretation of results from missions and dynamical models such as ours strongly relies on an improved understanding of physical phenomena that occur when meteoroids impact planetary surfaces. In our case we calculated the impact vaporization flux $\mathcal{F}$ using experimental and analytic work of Cintala (1992), yet the nature of this process might be more complex (e.g., Collette et al., 2014). Similar complexity might be expected in the calculation of the ejecta mass production rate M^+, where our calculation solely depends on the Koschny and Grün (2001) experiment, who used glass and nylon projectiles to produce hypervelocity (1–10 km/s) impact craters in ice-silicate mixture targets. However, the situation on the lunar surface is different. Both the lunar surface and the meteoroids impacting it are composed of different materials than used in the experiment of Koschny and Grün (2001). Meteoroids impacting the lunar surface have a wider velocity range. As discussed in Costello et al. (2018) the low surface hardness of the lunar regolith can dampen the ejecta production compared to harder surfaces usually available in laboratory impact experiments, such as that of Koschny and Grün (2001), used in this manuscript. All these differences might significantly change M^+ and decrease the current discrepancy between the model and LDEX observations in terms of the lunar dust cloud density n_0.

7. Summary and Conclusions

In this work we presented our dynamical model for the lunar meteoroid environment, which provides details about the orbital element distributions, directions, and velocities of meteoroids impacting the lunar surface. With this model we quantified the response of the surface to meteoroid impacts resulting in impact vaporization and ejecta mass production.

The model was first compared to measurements of the ejecta cloud surrounding the Moon both to establish its validity and to constrain the relative ratios of different meteoroid populations. Although our model is able to reproduce nightside observations of LADEE/LDEX, we found that the predicted dayside values were systematically smaller than those measured by LDEX. A linear increase of ejecta mass production rate from 6 AM to noon in lunar LT, convolved with our predicted meteoroid velocities and fluxes, provides significantly better agreement between our dynamical model and LDEX observations than if we assumed the soil response to be the same at day and night. Using the maximum linear increase of 60–80% at noon we were able to constrain the ratio of Halley-type and OCCs. This constraint is most sensitive to the SFD of meteoroids at their origin/source.

The absolute mass flux of meteoroids onto the Moon is unknown and measurements from Earth must be used as a reference point. Adopting the results reported by Carrillo-Sánchez et al. (2016), that is, that $\mathcal{M}_{\mathrm{JFC}} = 34.6$ t/day of meteoroids originating from JFCs arrive at Earth and the short-period comet to LPC mass flux ratio to be 6.92, we estimate that the HTC and OCC meteoroid mass flux at Earth is $\mathcal{M}_{\mathrm{HTC}} = 2.82 \pm 1.31$ t/day and $\mathcal{M}_{\mathrm{OCC}} = 2.18 \pm 1.31$ t/day, respectively. The total flux of main-belt asteroidal meteoroids cannot be constrained by modeling LDEX observations because they produce a negligible contribution to the total ejecta mass production rate due to their very low velocity. Thus, we adopted the meteoroid mass flux of MBAs to be $\mathcal{M}_{\mathrm{MBA}} = 3.7$ t/day at Earth. In order to stay consistent with Earth-based estimates of the mass flux ratio of short-period comet to LPC (Carrillo-Sánchez et al., 2016), we were forced to change the functional form of the ejecta mass production rate function, finding that it should be linearly proportional to the meteoroid mass flux. For different functional forms suggested by Koschny and Grün (2001) we found that the JFC meteoroids would dominate the ejecta mass production rates at Moon leading to the adoption of unacceptably small short-period comet to LPC mass flux ratios (~1–3) to fit the LDEX data, similar to the findings reported by Janches et al. (2018).

Using constraints from Earth and taking into account the gravitational focusing effects between Earth and the Moon, we conclude that the total mass accreted at the Moon is approximately $\mathcal{M}_{\mathrm{Moon}} = 1.4$ t/day assuming 43.3 t/day at Earth, where the individual contribution of meteoroid populations are: MBAs ~4.6%, JFCs ~72.6%, HTCs ~12.8%, and OCCs ~10.0%. This results in a short-period comet to LPC ratio ~2–3 times larger than the preliminary study of Janches et al. (2018) that represented one of many possible realizations

of the dynamical model that is able to fit available LDEX measurements. This work demonstrated that the solution space to provide a similar or better fit is wide due to the limited selenographic coverage of LADEE.

The resulting modeled direction and velocity distributions resemble results previously reported from meteor surveys at Earth (Figure 7) and preliminary reports of the model by Janches et al. (2018). The JFC meteoroids dominate the overall mass flux, are concentrated close to the ecliptic plane, and arrive from two directions: toward and away from the sun (helion/antihelion sources). HTC meteoroids populate the ring/toroidal structure around the apex and generate the apex source together with OCC meteoroids. MBA meteoroids due to their low relative velocity with respect to the Moon have radiants ranging from all directions and are hence able to populate the anti-apex source. The apex source represents the most energetic source of meteoroids with average impact velocities exceeding 55 km/s, while the toroidal and helion/antihelion sources are in general populated by meteoroids a factor of two slower. Due to the smaller gravitational focusing at the Moon, the JFC and MBAs meteoroids contribute 2.5 and 5 times less in terms of the mass flux to the lunar meteoroid environment, respectively, than at Earth. Due to a broad latitudinal distribution of cometary impactors the entire lunar surface can be exposed to impacts with velocities as high as 30 km/s, where the near ecliptic directions can produce impacts with velocities up to 72 km/s (Figure 9). This might have further consequences for possible excavation of volatile material from permanently shadowed polar craters and redistribution of such volatile material to their vicinity, although the ice reservoir for erosion through this fountain effect (Farrell et al., 2015) must be strictly surficial (∼1 mm), that is, exposed ice. We note that the most likely velocity of JFC and asteroidal meteoroids encountering the Moon is 9 km/s, and because these velocities produce incomplete vaporization of the impactors (Collette et al. (2014)), the Moon can act as a repository of composition of ancient meteoroids from these populations.

The meteoroid mass flux and, consequently, the impact vaporization flux and ejecta mass production rate experience yearly and monthly variations that can be well represented by a sum of two sine functions with periods of 1 year and 29.5 days (synodic period of the Moon). Yearly mass flux variations amount to 3.3% of the yearly average mass flux, while monthly variations amount to only 0.2%. These variations are larger for velocity-dependent quantities, where yearly variations of the impact vaporization flux account for 6–8%, while monthly variations are around 4–5%. When the full spectrum of impact velocities is taken into account, the apex/dawn terminator source is dominating both the impact vaporization flux and the ejecta mass production rate for any day of the year. If, however, impact velocities higher than 20 km/s lead to other phases (e.g., ionization or condensates), as suggested for Mercury (Pokorný et al., 2018), we predict that the meteor-driven source for the lunar neutral exosphere will demonstrate considerable variation in LT every month because then the midnight/noon sources dominate the impact vaporization flux. This prediction can be tested with LADEE Ultraviolet and Visible Spectrometer data. And because of the latitudinal dependence of impactor velocity, the atmosphere will also be more elongated in latitude in that case.

Experimental results from Koschny and Grün (2001) and our model were used to obtain absolute values of the impact mass production rates M^+ for the lunar surface (Figure 14), which yield a proxy of the gardening rate from meteoroids. Our results suggest that equatorial regions experience three to five times higher ejecta production—and thus gardening—rates than the polar regions. Different functional forms of the M^+ give variations of only 50% in this estimated parameter, which is smaller than the uncertainty imposed by our calibration based on Carrillo-Sánchez et al. (2016). Our model predicts lunar dust cloud density values higher by four orders of magnitude than those inferred by LDEX. This discrepancy might indicate that the ejecta mass production yield of lunar regolith is considerably lower than the experimental data used here. The estimated gardening rate is about 30 cm per million years from this range of meteoroids if we assume the Koschny and Grün (2001) yield.

Acknowledgments
P.P., D.J., and M.S.'s work was supported with NASA's SSO, LDAP, and ISFM awards. P.P. was partially supported by NASA's SSW award NNH14ZDA001N. P.P. would like to thank Laura Lenkić for enlightening discussions, useful comments, and thorough reads of the manuscript. J.R.S. was supported by NASA's Lunar Data Analysis Program (LDAP) grant 80NSSC17K0702. The data used to generate plots in this manuscript can be found online (https://github.com/McFly007/AstroWorks/tree/master/Pokorny_et_al_2019_JGR).

References

Barbieri, C., Benn, C. R., Cremonese, G., Verani, S., & Zin, A. (2001). Meteor showers on the lunar atmosphere. *Earth Moon and Planets*, *85*, 479–486.

Berezhnoy, A. A. (2013). Chemistry of impact events on the Moon. *Icarus*, *226*, 205–211. https://doi.org/10.1016/j.icarus.2013.05.030

Blaauw, R. C., Campbell-Brown, M. D., & Weryk, R. J. (2011). Mass distribution indices of sporadic meteors using radar data. *Monthly Notices of the Royal Astronomical Society*, *412*(2033–2039). https://doi.org/10.1111/j.1365-2966.2010.18038.x

Borin, P., Cremonese, G., Marzari, F., & Lucchetti, A. (2017). Asteroidal and cometary dust flux in the inner solar system. *Astronomy & Astrophysics*, *605*, A94. https://doi.org/10.1051/0004-6361/201730617

Borkowski, K. J., & Dwek, E. (1995). The fragmentation and vaporization of dust in grain-grain collisions. *The Astrophysical Journal*, *454*, 254. https://doi.org/10.1086/176480

Bruno, M., Cremonese, G., & Marchi, S. (2007). Neutral sodium atoms release from the surfaces of the Moon and Mercury induced by meteoroid impacts. *Planetary and Space Science*, *55*, 1494–1501. https://doi.org/10.1016/j.pss.2006.10.006

Burns, J. A., Lamy, P. L., & Soter, S. (1979). Radiation forces on small particles in the solar system. *Icarus*, *40*, 1–48. https://doi.org/10.1016/0019-1035(79)90050-2

Campbell-Brown, M. D. (2008). High resolution radiant distribution and orbits of sporadic radar meteoroids. *Icarus*, *196*, 144–163. https://doi.org/10.1016/j.icarus.2008.02.022

Carrillo-Sánchez, J. D., Nesvorný, D., Pokorný, P., Janches, D., & Plane, J. M. C. (2016). Sources of cosmic dust in the Earth's atmosphere. *Geophysical Research Letters*, *43*, 11. https://doi.org/10.1002/2016GL071697

Cintala, M. J. (1992). Impact-induced thermal effects in the lunar and Mercurian regoliths. *Journal of Geophysical Research*, *97*, 947–973. https://doi.org/10.1029/91JE02207

Colaprete, A., Sarantos, M., Wooden, D. H., Stubbs, T. J., Cook, A. M., & Shirley, M. (2016). How surface composition and meteoroid impacts mediate sodium and potassium in the lunar exosphere. *Science*, *351*, 249–252. https://doi.org/10.1126/science.aad2380

Collette, A., Sternovsky, Z., & Horanyi, M. (2014). Production of neutral gas by micrometeoroid impacts. *Icarus*, *227*, 89–93. https://doi.org/10.1016/j.icarus.2013.09.009

Costello, E. S., Ghent, R. R., & Lucey, P. G. (2018). The mixing of lunar regolith: Vital updates to a canonical model. *Icarus*, *314*, 327–344. https://doi.org/10.1016/j.icarus.2018.05.023

Cremonese, G., Borin, P., Lucchetti, A., Marzari, F., & Bruno, M. (2013). Micrometeoroids flux on the Moon. *Astronomy and Astrophysics*, *551*, A27. https://doi.org/10.1051/0004-6361/201220541

Cremonese, G., Borin, P., Martellato, E., Marzari, F., & Bruno, M. (2012). New calibration of the micrometeoroid flux on Earth. *The Astrophysical Journal Letters*, *749*, L40. https://doi.org/10.1088/2041-8205/749/2/L40

Dohnanyi, J. S. (1969). Collisional model of asteroids and their debris. *Journal of Geophysical Research*, *74*, 2531–2554. https://doi.org/10.1029/JB074i010p02531

Farrell, W. M., Hurley, D. M., & Zimmerman, M. I. (2015). Spillage of lunar polar crater volatiles onto adjacent terrains: The case for dynamic processes. *Geophysical Research Letters*, *42*, 3160–3165. https://doi.org/10.1002/2015GL063200

Fentzke, J. T., & Janches, D. (2008). A semi-empirical model of the contribution from sporadic meteoroid sources on the meteor input function in the MLT observed at Arecibo. *Journal of Geophysical Research*, *113*, A03304. https://doi.org/10.1029/2007JA012531

Feroz, F., & Hobson, M. P. (2008). Multimodal nested sampling: An efficient and robust alternative to Markov Chain Monte Carlo methods for astronomical data analyses. *Monthly Notices of the Royal Astronomical Society*, *384*, 449–463. https://doi.org/10.1111/j.1365-2966.2007.12353.x

Feroz, F., Hobson, M. P., & Bridges, M. (2009). MULTINEST: An efficient and robust Bayesian inference tool for cosmology and particle physics. *Monthly Notices of the Royal Astronomical Society*, *398*, 1601–1614. https://doi.org/10.1111/j.1365-2966.2009.14548.x

Feroz, F., Hobson, M. P., Cameron, E., & Pettitt, A. N. (2013). Importance nested sampling and the MultiNest algorithm. ArXiv e-prints.

Fulle, M., Colangeli, L., Mennella, V., Rotundi, A., & Bussoletti, E. (1995). The sensitivity of the size distribution to the grain dynamics: Simulation of the dust flux measured by GIOTTO at P/Halley. *Astronomy and Astrophysics*, *304*, 622.

Fulle, M., Marzari, F., Della Corte, V., Fornasier, S., Sierks, H., Rotundi, A., et al. (2016). Evolution of the dust size distribution of comet 67p/Churyumov-Gerasimenko from 2.2 AU to perihelion. *The Astrophysical Journal*, *821*, 19. https://doi.org/10.3847/0004-637X/821/1/19

Gault, D. E. (1973). Displaced mass, depth, diameter, and effects of oblique trajectories for impact craters formed in dense crystalline rocks. *Moon*, *6*, 32–44. https://doi.org/10.1007/BF02630651

Green, S. F., McBride, N., Colwell, M. T. S. H., McDonnell, J. A. M., Tuzzolino, A. J., Economou, T. E., et al. (2007). Stardust Wild 2 dust measurements. *Dust in Planetary Systems*, *643*, 35–44.

Greenberg, R. (1982). Orbital interactions—A new geometrical formalism. *The Astronomical Journal*, *87*, 184–195. https://doi.org/10.1086/113095

Grun, E., Zook, H. A., Fechtig, H., & Giese, R. H. (1985). Collisional balance of the meteoritic complex. *Icarus*, *62*, 244–272. https://doi.org/10.1016/0019-1035(85)90121-6

Horányi, M., Szalay, J. R., Kempf, S., Schmidt, J., Grün, E., Srama, R., & Sternovsky, Z. (2015). A permanent, asymmetric dust cloud around the Moon. *Nature*, *522*, 324–326. https://doi.org/10.1038/nature14479

Janches, D., Close, S., Hormaechea, J. L., Swarnalingam, N., Murphy, A., O'Connor, D., et al. (2015). The Southern Argentina Agile MEteor Radar Orbital System (SAAMER-OS): An initial sporadic meteoroid orbital survey in the southern sky. *The Astrophysical Journal*, *809*, 36. https://doi.org/10.1088/0004-637X/809/1/36

Janches, D., Pokorný, P., Sarantos, M., Szalay, J. R., Horányi, M., & Nesvorný, D. (2018). Constraining the ratio of micrometeoroids from short- and long-period comets at 1 au from LADEE observations of the lunar dust cloud. *Geophysical Research Letters*, *45*, 1713–1722. https://doi.org/10.1002/2017GL076065

Janches, D., Swarnalingam, N., Carrillo-Sanchez, J. D., Gomez-Martin, J. C., Marshall, R., Nesvorný, D., et al. (2017). Radar detectability studies of slow and small zodiacal dust cloud particles. III. The role of sodium and the head echo size on the probability of detection. *The Astrophysical Journal*, *843*, 1. https://doi.org/10.3847/1538-4357/aa775c

Jenniskens, P., Nénon, Q., Gural, P. S., Albers, J., Haberman, B., Johnson, B., et al. (2016). CAMS newly detected meteor showers and the sporadic background. *Icarus*, *266*, 384–409. https://doi.org/10.1016/j.icarus.2015.11.009

Kessler, D. J. (1981). Derivation of the collision probability between orbiting objects: The lifetimes of Jupiter's outer moons. *Icarus*, *48*, 39–48. https://doi.org/10.1016/0019-1035(81)90151-2

Kortenkamp, S. J. (2013). Trapping and dynamical evolution of interplanetary dust particles in Earth's quasi-satellite resonance. *Icarus*, *226*, 1550–1558. https://doi.org/10.1016/j.icarus.2013.08.020

Koschny, D., & Grün, E. (2001). Impacts into ice-silicate mixtures: Ejecta mass and size distributions. *Icarus*, *154*, 402–411. https://doi.org/10.1006/icar.2001.6708

Krivov, A. V., Sremčević, M., Spahn, F., Dikarev, V. V., & Kholshevnikov, K. V. (2003). Impact-generated dust clouds around planetary satellites: Spherically symmetric case. *Planetary and Space Science*, *51*, 251–269. https://doi.org/10.1016/S0032-0633(02)00147-2

Kuchner, M. J., & Stark, C. C. (2010). Collisional grooming models of the Kuiper Belt dust cloud. *The Astronomical Journal*, *140*, 1007–1019. https://doi.org/10.1088/0004-6256/140/4/1007

Leinert, C., Richter, I., Pitz, E., & Planck, B. (1981). The zodiacal light from 1.0 to 0.3 A.U. as observed by the HELIOS space probes. *Astronomy and Astrophysics*, *103*, 177–188.

Love, S. G., & Brownlee, D. E. (1993). A direct measurement of the terrestrial mass accretion rate of cosmic dust. *Science*, *262*, 550–553. https://doi.org/10.1126/science.262.5133.550

McNamara, H., Jones, J., Kauffman, B., Suggs, R., Cooke, W., & Smith, S. (2004). Meteoroid engineering model (MEM): A meteoroid model for the inner solar system. *Earth, Moon, and Planets*, *95*, 123–139. https://doi.org/10.1007/s11038-005-9044-8

Merkel, A. W., Cassidy, T. A., Vervack, R. J., McClintock, W. E., Sarantos, M., Burger, M. H., & Killen, R. M. (2017). Seasonal variations of Mercury's magnesium dayside exosphere from MESSENGER observations. *Icarus*, *281*, 46–54. https://doi.org/10.1016/j.icarus.2016.08.032

Morgan, T. H., & Killen, R. M. (1997). A non-stoichiometric model of the composition of the atmospheres of Mercury and the Moon. *Planetary and Space Science*, *45*, 81. https://doi.org/10.1016/S0032-0633(96)00099-2

Morgan, T. H., Zook, H. A., & Potter, A. E. (1988). Impact-driven supply of sodium and potassium to the atmosphere of Mercury. *Icarus*, *75*, 156–170. https://doi.org/10.1016/0019-1035(88)90134-0

Morris, R. V. (1978). In situ reworking /gardening/ of the lunar surface—Evidence from the Apollo cores. In *Lunar and planetary science conference proceedings*, *9*, New York, pp. 1801–1811.

Nesvorný, D., Janches, D., Vokrouhlický, D., Pokorný, P., Bottke, W. F., & Jenniskens, P. (2011). Dynamical model for the zodiacal cloud and sporadic meteors. *The Astrophysical Journal*, *743*, 129. https://doi.org/10.1088/0004-637X/743/2/129

Nesvorný, D., Jenniskens, P., Levison, H. F., Bottke, W. F., Vokrouhlický, D., & Gounelle, M. (2010). Cometary origin of the zodiacal cloud and carbonaceous micrometeorites. Implications for hot debris disks. *The Astrophysical Journal*, *713*, 816–836. https://doi.org/10.1088/0004-637X/713/2/816

Nesvorný, D., Vokrouhlický, D., Pokorný, P., & Janches, D. (2011). Dynamics of dust particles released from Oort cloud comets and their contribution to radar meteors. *The Astrophysical Journal*, *743*, 37. https://doi.org/10.1088/0004-637X/743/1/37

Öpik, E. J. (1951). Collision probability with the planets and the distribution of planetary matter. *Proceedings of the Royal Irish Academy. Section A*, *54*, 165–199.

Pokorný, P., & Brown, P. G. (2016). A reproducible method to determine the meteoroid mass index. *Astronomy and Astrophysics*, *592*, A150. https://doi.org/10.1051/0004-6361/201628134

Pokorný, P., Janches, D., Brown, P. G., & Hormaechea, J. L. (2017). An orbital meteoroid stream survey using the Southern Argentina Agile MEteor Radar (SAAMER) based on a wavelet approach. *Icarus*, *290*, 162–182. https://doi.org/10.1016/j.icarus.2017.02.025

Pokorný, P., Sarantos, M., & Janches, D. (2018). A comprehensive model of the meteoroid environment around Mercury. *The Astrophysical Journal*, *863*, 31. https://doi.org/10.3847/1538-4357/aad051

Pokorný, P., & Vokrouhlický, D. (2013). Öpik-type collision probability for high-inclination orbits: Targets on eccentric orbits. *Icarus*, *226*, 682–693. https://doi.org/10.1016/j.icarus.2013.06.015

Pokorný, P., Vokrouhlický, D., Nesvorný, D., Campbell-Brown, M., & Brown, P. (2014). Dynamical model for the toroidal sporadic meteors. *The Astrophysical Journal*, *789*, 25. https://doi.org/10.1088/0004-637X/789/1/25

Poppe, A. R. (2016). An improved model for interplanetary dust fluxes in the outer Solar System. *Icarus*, *264*, 369–386. https://doi.org/10.1016/j.icarus.2015.10.001

Rickman, H., Wiśniowski, T., Wajer, P., Gabryszewski, R., & Valsecchi, G. B. (2014). Monte Carlo methods to calculate impact probabilities. *Astronomy and Astrophysics*, *569*, A47. https://doi.org/10.1051/0004-6361/201423966

Rotundi, A., Sierks, H., Della Corte, V., Fulle, M., Gutierrez, P. J., Lara, L., et al. (2015). Dust measurements in the coma of comet 67P/Churyumov-Gerasimenko inbound to the Sun. *Science*, *347*(1), aaa3905. https://doi.org/10.1126/science.aaa3905

Sarantos, M., Killen, R. M., Glenar, D. A., Benna, M., & Stubbs, T. J. (2012). Metallic species, oxygen and silicon in the lunar exosphere: Upper limits and prospects for LADEE measurements. *Journal of Geophysical Research*, *117*, A03103. https://doi.org/10.1029/2011JA017044

Sarantos, M., Killen, R. M., Surjalal Sharma, A., & Slavin, J. A. (2010). Sources of sodium in the lunar exosphere: Modeling using ground-based observations of sodium emission and spacecraft data of the plasma. *Icarus*, *205*, 364–374. https://doi.org/10.1016/j.icarus.2009.07.039

Smith, S. M., Wilson, J. K., Baumgardner, J., & Mendillo, M. (1999). Discovery of the distant lunar sodium tail and its enhancement following the Leonid Meteor Shower of 1998. *Geophysical Research Letters*, *26*, 1649–1652. https://doi.org/10.1029/1999GL900314

Steel, D. I., & Baggaley, W. J. (1985). Collisions in the solar system—I. Impacts of the Apollo-Amor-Aten asteroids upon the terrestrial planets. *Monthly Notices of the Royal Astronomical Society*, *212*, 817–836. https://doi.org/10.1093/mnras/212.4.817

Steel, D. I., & Elford, W. G. (1986). Collisions in the solar system—III. Meteoroid survival times. *Monthly Notices of the Royal Astronomical Society*, *218*, 185–199. https://doi.org/10.1093/mnras/218.2.185

Suggs, R. M., Moser, D. E., Cooke, W. J., & Suggs, R. J. (2014). The flux of kilogram-sized meteoroids from lunar impact monitoring. *Icarus*, *238*, 23–36. https://doi.org/10.1016/j.icarus.2014.04.032

Szalay, J. R., & Horányi, M. (2015). Annual variation and synodic modulation of the sporadic meteoroid flux to the Moon. *Geophysical Research Letters*, *42*, 10. https://doi.org/10.1002/2015GL066908

Szalay, J. R., & Horányi, M. (2016). Lunar meteoritic gardening rate derived from in situ LADEE/LDEX measurements. *Geophysical Research Letters*, *43*, 4893–4898. https://doi.org/10.1002/2016GL069148

Szalay, J. R., Horányi, M., Colaprete, A., & Sarantos, M. (2016). Meteoritic influence on sodium and potassium abundance in the lunar exosphere measured by LADEE. *Geophysical Research Letters*, *43*, 6096–6102. https://doi.org/10.1002/2016GL069541

Szalay, J. R., Pokorný, P., Jenniskens, P., & Horányi, M. (2018). Activity of the 2013 Geminid meteoroid stream at the Moon. *Monthly Notices of the Royal Astronomical Society*, *474*, 4225–4231. https://doi.org/10.1093/mnras/stx3007

Vokrouhlický, D., Pokorný, P., & Nesvorný, D. (2012). Öpik-type collision probability for high-inclination orbits. *Icarus*, *219*, 150–160. https://doi.org/10.1016/j.icarus.2012.02.021

Wetherill, G. W. (1967). Collisions in the asteroid belt. *Journal of Geophysical Research*, *72*, 2429. https://doi.org/10.1029/JZ072i009p02429

Wurz, P., Rohner, U., Whitby, J. A., Kolb, C., Lammer, H., & Dobnikar, P. (2007). The lunar exosphere: The sputtering contribution, Martín-Fernández, J. A., pp. 486–496. https://doi.org/10.1016/j.icarus.2007.04.034

Yang, H., Ishiguro, M., & 173 (2018). Evolution of cometary dust particles to the orbit of the Earth: Particle size, shape, and mutual collisions. *The Astrophysical Journal*, *854*. https://doi.org/10.3847/1538-4357/aaab59

Zuber, M. T., Head, J. W., Smith, D. E., Neumann, G. A., Mazarico, E., Torrence, M. H., et al. (2012). Constraints on the volatile distribution within Shackleton crater at the lunar south pole. *Nature*, *486*, 378–381. https://doi.org/10.1038/nature11216